STUDY OF MICROWAVE DOSIMETRY

by

Eugene F. Knott
The University of Michigan
Radiation Laboratory
2455 Hayward St.
Ann Arbor, Michigan 48105

July 1972

Final Technical Report
Contract No. NIH-71-2373

Project Officer: Dr. Donald I. McRee

10531-1-F = RL-2198

Prepared For

National Institute of Environmental Health Sciences
National Institute of Health
Research Triangle Park, North Carolina 27209

FOREWORD

This is the final report summarizing the research carried out by the University of Michigan Radiation Laboratory for the National Institute of Environmental Health Sciences, National Institute of Health. The research was entitled "Study of Microwave Dosimetry" and was carried out under Contract Number NIH-71-2373; the contract period was from June 29, 1971 through June 28, 1972.

The contract objective was "to develop techniques and detectors using electric and magnetic probe technology which can be used to measure the energy absorbed in a biological specimen placed in either near or far microwave fields of frequencies ranging from 1 GHz to 10 GHz."

ABSTRACT

Electromagnetic probes are especially useful in microwave dosimetry if they are implantable. The shielded loop probe is a promising candidate because its shape and size are compatible with implantation and because its induced voltage is independent of the surrounding medium. Like any other probe, however, the intrinsic impedance of the loop depends upon the electrical characteristics of the surrounding medium and unless the detector driven by the probe has infinite impedance, the detector output signal will show a related dependence.

This report describes a test program in which six shielded loop probes were exposed to microwave fields in both air and in simulated biological materials. Frequencies from 1.0 to 10.0 GHz were used and in order to determine the induced loop voltages, measurements of both the detector and probe impedances were made. The research shows that at these frequencies and because of the influence of the medium surrounding the probe, implantable broadband probes will be difficult to produce and that the entire probe system (including output display equipment) should be included in the calibration procedure.

TABLE OF CONTENTS

I
INTRODUCTION

1.1 General Remarks

It has been well documented that microwave radiation can induce changes in biological systems and in many cases these changes are lethal. Detrimental biological effects are hazardous if they occur in people or can be beneficial if they affect pests or parasites. In either event, however, the quantitative relation between cause and effect has not been firmly established; i.e., the dose or dose parameters have not been defined.

In microwave irradiation studies, the power density of the incident radiation has been favored as the parameter characterizing the exposure. It is usually measured in the absence of the specimen and, unless the experiments are carried out within a closed system such as a cavity, the incident power density is probably unaffected by the presence or absence of the specimen. On the other hand, the total power flowing into the volume occupied by the specimen most assuredly depends whether or not the subject is present. Thus, while a specification of the incident power density in the absence of the specimen in all likelihood correctly describes the incident power density in the presence of the specimen, it does not specify the internal fields or power flux.

It is natural to regard power density as a dose parameter, since it seems to require energy to bring about biological changes and energy is an accumulation (over time) of power. Unfortunately, energy or power densities are extremely difficult quantities to measure inside a biological specimen, or any other dielectric medium. If we could be assured that all absorbed energy is converted to heat (with none taken up in biochemical reactions, for example), and if the temperature rise is large enough, the energy absorbed could be determined by a series of temper-

ature measurements. But if the temperature rise is not measurable, as may be the case for low-level irradiation, then other means are required. Basically an electromagnetic probe is required.

A probe is nothing more than a small antenna whose output signal can be related to field intensity or power density. Several commercial firms have developed microwave probes, among them Narda Microwave Corporation and General Microwave Corporation, but the most notable contribution has come from the National Bureau of Standards (Bowman, et al, 1970). The probes invariably consist of one or more electric dipoles and the metering equipment is usually calibrated in terms of power density, milliwatts or microwatts per square centimeter, for example. The probes are currently much too large to be implantable, but this may not be true for long, because probe development is advancing rapidly. The production of a useful probe requires that it be calibrated, of course, and calibration is invariably carried out in a free space environment.

In our contract with the National Institute of Environmental Health Sciences, the Radiation Laboratory undertook a probe development program that was quite different in two important respects: our probes are implantable and we sought to calibrate them when immersed in dielectrics with properties similar to those of biological materials. Since the probes are very small, they respond essentially to the field intensity at a point and, this being so, they are equally useful in both near and far field situations. Although the specimen may not be uniformly illuminated when in the near field, and although the fields may have both transverse and radial components (not all of which decay as $1/r$), a probe does not know this; it obligingly responds to the components of the total field intensity normal to the plane of the loop. Our probes are shielded magnetic loop probes and, as such, the induced loop voltage is independent of the medium surrounding the probe.

In all fairness, we must list the limitations of the probes as well as their

virtues. The probes were RF probes in the sense that the RF signal was fed to an external detector located some distance from the loop itself. This meant that the probe lead had to be metallic in order to preserve the signal strength, and the presence of conductors in the field being probed can influence (perturb) the field. Since the probes were small, the output signals were weak and sensitive detection equipment had to be used. And although we knew the field polarizations for our test procedures, and could thus orient the probes correctly, the polarizations in a complicated, unknown material would require more extensive manipulation. Yet one might legitimately inquire if polarization is not an important characteristic of the field in certain instances. For example, is a neuron more sensitive to fields parallel or transverse to its length?

It might be argued that our probes do not respond to absorbed energy or power, yet this is true of any other electromagnetic probe calibrated in terms of field or power intensity. Absorbed power can be measured only by noting the change in power density from point to point in the material, and then even a power-sensitive probe may not necessarily yield the correct results. In principle, the only way to accomplish this task is to measure the complex (amplitude and phase) tangential electric and magnetic field distributions over an entire surface enclosing the volume of concern.

The field of microwave dosimetry is still evolving and we cannot yet state what might be the appropriate dose parameter. As noted above, power density has been favored thus far, with field intensity seldom noted, but this is because it is the incident power that is measured. In free space one is as good as the other because the relations between them (i.e., the impedance of free space, 377 ohms) is known. But as attention is increasingly directed toward the actual fields or power intensity within an irradiated specimen, the field strength may prove to be a more important parameter than the power intensity, especially if power levels are so low that exposure is measured in days of weeks instead of minutes. It is therefore

necessary that we develop the capability of measuring field intensity inside biological specimens.

Our test results indicate, but do not conclusively prove, that the induced loop voltage of a magnetic probe is independent of the medium in which the probe is immersed. The data are clustered near the value that might be expected from theory, yet the spread in results is uncomfortably large. Expectedly, the results for the power frequencies are more consistent than those obtained for the higher frequencies. In many cases there is a strong correlation between the probe impedance (a measurement required for calibration when the probe is immersed in a dielectric medium) and the probe calibration coefficient, suggesting that these measurements must be performed carefully. In spite of the lack of more consistent results, we remain convinced that probe response is faithfully predicted by Faraday's law.

1.2 Overall Test Plan

The details of the test plan are given in Chapter III, but the plan is essentially to measure the relationship between the magnetic flux to which a probe is exposed and the voltage induced in the probe by the flux. Since theory indicates that this voltage is independent of the medium, we planned to carry out the measurements in three different media to see to what degree this is true. The testing was to have been carried out with dielectrics having electrical properties similar to typical biological materials, but since the artificial dielectrics were not always chemically and physically stable over a span of several months, we eventually settled on materials with somewhat different electrical, but more stable physical, properties.

To guard against the hazard of having to repeat the entire test sequence due to the accidental loss of a probe, we constructed several of them. The probes are delicate and because the testing required extensive connecting and disconnecting of probe from mating connectors, the possibility of damaging a probe was always with us. Of the eight probes assembled early in the program, six were used for

the entire test program. Since all six were of virtually the same size, this also permitted us to compare individual probe responses; as will be shown in Chapter IV, some probes behaved much better than others, but unfortunately we cannot determine why. Chapter II explains how the shielded loop probes were constructed; a stereomicroscope is necessary because of the small size of the loops.

We had planned to test the probes in both an enclosed transmission line and in an open, free space environment to verify the probe behavior in "near" and "far" field conditions. Unfortunately, due to complications in the field structure in the transmission line, there was only one frequency for which we have results obtained under both conditions. Perhaps expectedly, the data acquired in the enclosed system tests seem more consistent than those obtained in the open system.

The transmission line section for the enclosed system tests had to be large enough that our probes could be inserted in it and exposed to the fields inside. The ideal line seemed to be Hewlett-Packard Model 805-C slab line, since it has a wide slot, yet supports a TEM (transverse electromangetic) wave. With the slab line we could avoid the necessity of using several waveguide sample holders (one for each frequency band) as well as obviate the need to drill holes in the waveguide to receive the probes. The mathematical description of the field structure within the line turned out to be fairly complicated, even for the TEM mode, as might be appreciated from the derivation in Appendix B.

In order to show how shielded magnetic loop probes work, we include in Appendix A a detailed derivation of the induced voltage due to an alternating flux threading the loop. If the loop is small enough in terms of wavelengths measured in the surrounding medium, and if the loop supports only filamentary currents, then the induced voltage can be related to the magnetic flux density by a very simple formula. On the other hand, the intrinsic loop impedance is a very complicated quantity to evaluate theoretically, and, in fact, we measure it rather than embark on a complex computational task. At higher frequencies for which the loop is no longer electrically

small, the simple formula breaks down.

Having been the first to attempt to calibrate probes in lossy dielectrics for use in microwave dosimetry, we may also claim the distinction of having made the first mistakes. With an eye toward the future, and supported by the benefits of experience, we summarize in Chapter V the difficulties of such calibration and how the work may be more fruitfully extended in the future.

1.3 Summary

The heavy mathematics in this final report have been relegated to appendices because it is the result, not the derivation, that is important. The derivations are neither rigorous nor elegant in a mathematical sense, but form sufficient physical foundation for the probe calibration tests. To the practical reader who may wish to construct his own probes or his own dielectric materials, we commend Chapter II. Chapter III is a detailed exposition of the probe testing procedure and Chapter IV summarizes the results. Our conclusions and recommendations may be found in Chapter V.

II

PROBES AND MATERIALS

In this chapter we describe some of the practical aspects of the research. The construction of small shielded loop probes is nearly as much art as it is science and it requires several attempts before an individual acquires the experience necessary to produce an acceptable probe. In section 2.1 we describe the elements of probe construction and give some helpful little hints learned from past experience.

In section 2.2 we explain some of the difficulties encountered in producing the synthetic biological materials to be used in the probe testing. A good sample of synthetic bone was obtained by using Professor Guy's recipe, but his synthetic muscle recipe was unsuitable for our needs. Instead we bought a piece of commercial absorbing material whose properties (according to the manufacturer) were close to those of Guy's synthetic muscle. The dielectric constant of this material turned out to be lower than expected, so we merely regarded it as synthetic brain material instead.

The bone and brain substitutes were rigid and we machined them into rectangular slabs to fit our transmission line sample holder for the enclosed system measurements. Rather than try to machine these materials into spheres for the far field measurements, we purchased a pair of hard rubber handballs in a sporting goods shop. One was destroyed to obtain a sample for measurement of dielectric constant and the other was drilled with a hole to receive a bent probe. The dielectric constant of these spheres put them in the synthetic bone category. (The spherical shape was necessary for reasons given later, in Chapter III). The method by which the dielectric constants were measured is described in section 2.3.

2.1 Probe Construction Techniques

We decided early in the research that it would be prudent to start the test program with several probes, instead of only one or two, so that enough probes would still remain to complete the evaluation in case a probe might be accidentally damaged. Although several probes were already on hand from other investigations, we built six more, striving to make them as much alike as possible. Preliminary electrical tests showed that one of them was irreparably damaged, whereupon we made another one to replace it. Of all the probes, both new and old, we selected six as test candidates. Initial testing indicated substantial differences in the sensitivities of the probes to the same field strength, and although further systematic testing showed the variations to be less than was seen at first, differences in probe response were still noted.

Figure 2-1 is a photograph of the six probes. Three of them are "bent" probes whose loops have been bent at right angles to the probe lead, and these probes are therefore most sensitive to magnetic fields parallel to the probe lead. The bent probes were named D, E and M, and their names were written on small flags of Scotch tape affixed to the probes near the connector end. The remaining three probes were "straight" probes having their loops parallel to the probe lead like tennis rackets. The straight probes show maximum response when the plane of the loop is parallel to the direction of propagation of the incident wave, with the electric field polarized along the probe lead. When the plane of the loop is broadside to the incident field, the straight probes should theoretically have no output signal. These probes were named C, I and F. Probes D and E were old probes remaining from previous investigations and M, C, I and F were new. Probes H and K were constructed during the contract, but were never used.

Some steps in the construction of a probe are best carried out on the stage of a stereomicroscope. In addition it is helpful to have a small anvil built and

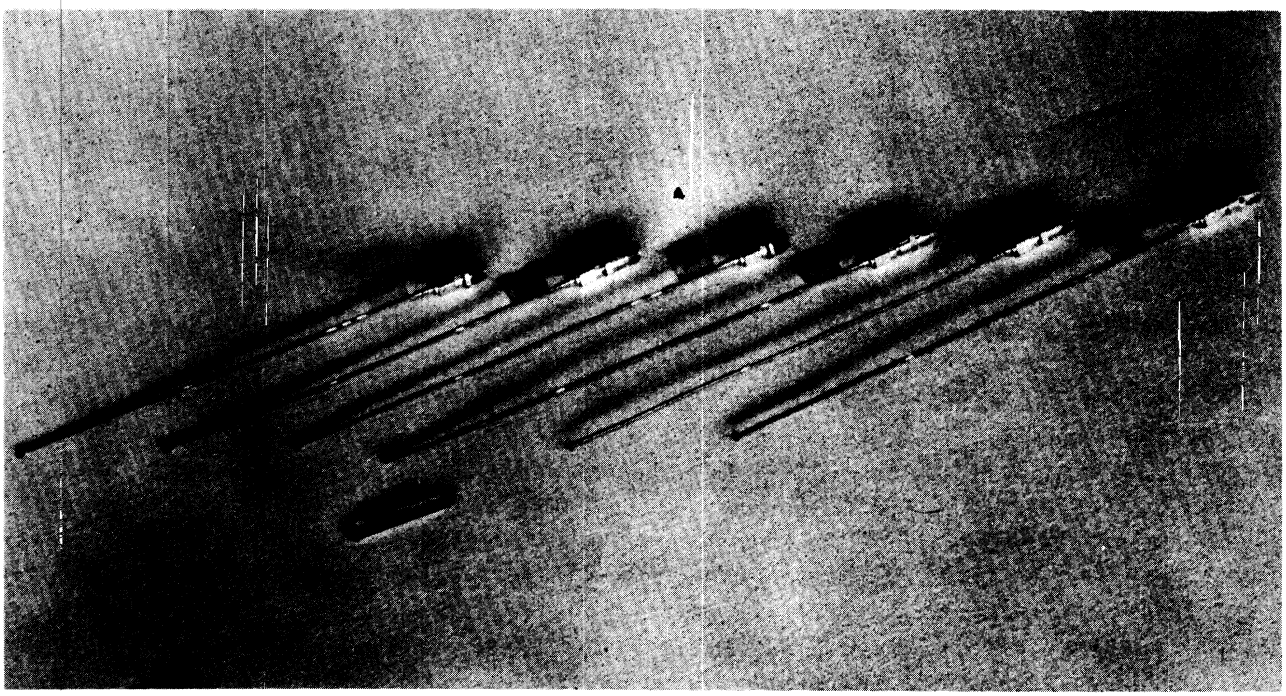

Figure 2-1. These six probes were evaluated; note their name tags.

fastened to a heavy plate, since it is often necessary to rest the probe on a solid elevated surface during soldering operations and while the gap is being cut in the outer conductor. A few double-edged razor blades and some strips of brass shim stock are necessary for some of the operations, as will be shown in a moment.

The probes are made from small semi-rigid coaxial line, which is available in random lengths up to 20 feet long from Uniform Tubes, Inc., Collegeville, Pennsylvania. The outer conductor is copper, having an outer diameter of 0.022 inch and the inner conductor is silver plated, copper-clad steel with a diameter of 0.005 inch. Although Uniform Tubes specifies that the minimum bend radius of the coaxial line is about 1/16 inch, we have consistently made loops with nearly half this radius. The dielectric material of the line is teflon.

The first step in probe construction is to obtain a piece of the semi-rigid line 6 to 8 inches long. Next the loop is formed by wrapping about $1\frac{1}{4}$ turns of the line around a small rod as shown in Figure 2-2(a). We have had consistently good results using the shank of a No. 51 drill with a diameter of 0.067 inch. Next a line is scoured around the outer conductor with a razor blade near the point where the loop crosses itself. This is a meticulous operation, since care must be taken to sever only the outer conductor. The operation, if successful, makes it possible to slip the outer conductor off the extra quarter turn, thus exposing the teflon dielectric.

The dielectric must now be parted down to the slender inner conductor, so that it too may be slipped off, but a razor blade is too sharp a tool to do this because it may slice off the center conductor along with the dielectric. A better method is to use a sharpened piece of brass shim stock, since brass is softer than the steel center conductor. After the teflon has been cut all the way around, it may be slipped off, exposing 3 or 4 mm of the inner conductor. The exposed center conductor should then be wrapped around the outer conductor of the line at the crossover point, as shown in Figure 2-2(b).

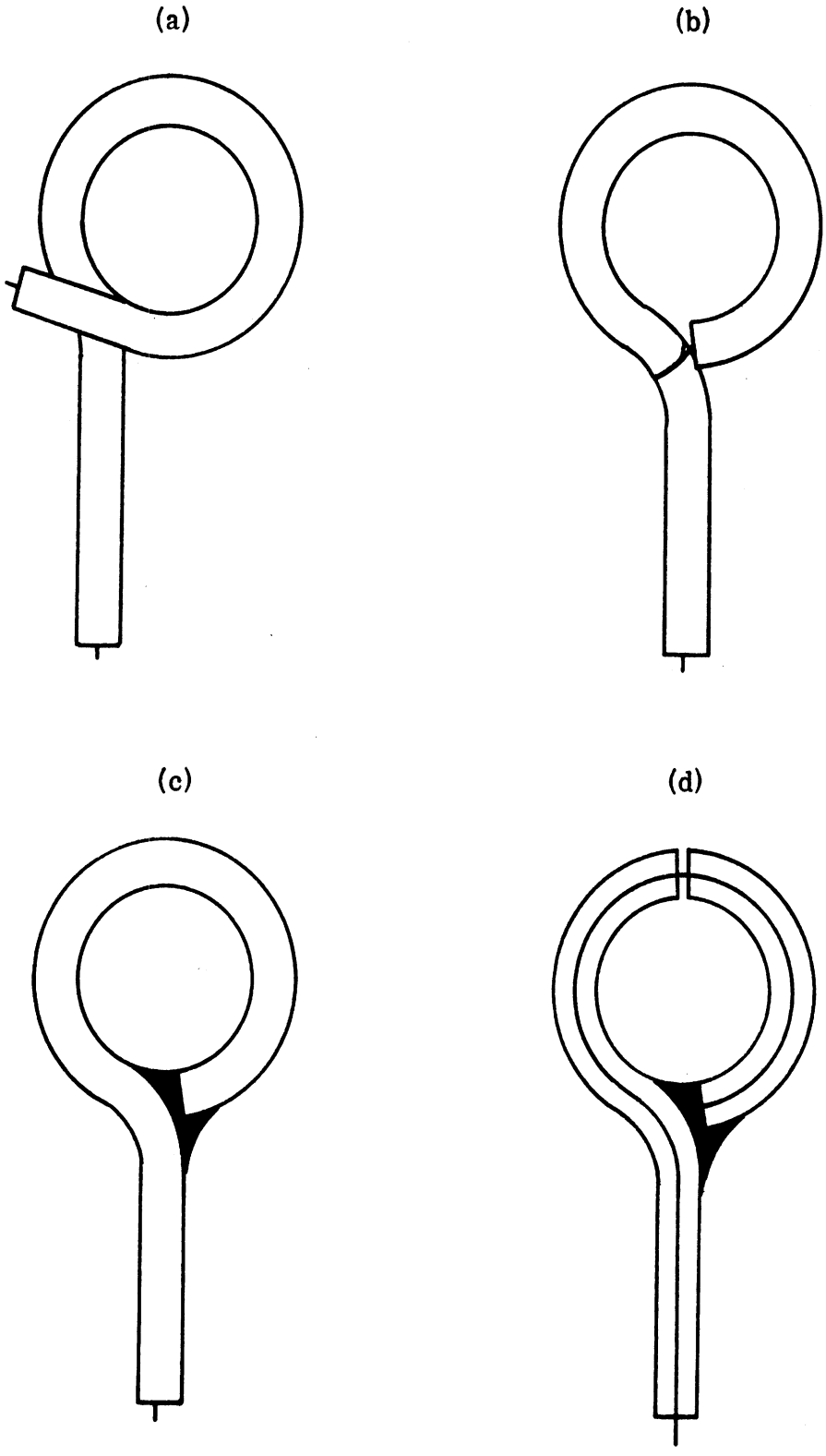

Figure 2-2. Probe construction sequence.

To insure a good electrical contact between the inner and outer conductor, and to strengthen the loop itself, it is necessary to apply a blob of solder as in Figure 2-2(c). The application of heat must be minimized because the teflon has a high thermal coefficient of expansion and tends to extrude out of the exposed end of the line. After trying several types of solder, including low melting solder and even conducting expoxy, we found that the ordinary rosin core solder used in electronic work worked best if applied quickly.

Next a gap must be cut around the outer conductor as shown in Figure 2-2(d). The best tool for this is a razor blade deliberately broken so as to have a sharp thin tip with the cutting edge running all the way to the tip. The broken blade must be be narrow enough to be slipped into the loop to cut the inner portion of the outer conductor. With a gentle sawing motion, the blade is used to cut a very narrow slot running all the way around the outer conductor.

The gap-cutting process produces tiny fragments of copper that bridge the gap and these should be removed. We tried using a hair from a soft brush to clean the gap, but the hair is usually larger than the gap and does not clear away the metal particles. A better method is to immerse the loop in a thimble filled with solvent such as acetone or alcohol, and using an eyedropper (also immersed in the solvent), to force the solvent back and forth over the gap. When the gap is clear, the loop should be coated with a protective covering of enamel or glue, or, indeed, anything that will keep foreign particles from clinging to and bridging the gap. The gap of a finished probe is so narrow that it is difficult to see with the unaided eye. Figure 2-3 is a close-up photograph of probe C showing the loop protected by a hardened drop of varnish. This probe has a fine gap, but due to reflections of lamps used to light the probe for the photograph the entire gap cannot be seen.

There are several connectors available to attach to the output end of the probe, including slip-on or screw-on connectors, but the latter tend to be more reliable. The particular connector we used is Omni-Spectra's plug, model OSSM 551-1,

Figure 2-3. Close-up of probe C compared with a common straight pin.

designed for braided cable. The connector has four parts but when used on the 0.022-inch diameter rigid line, two of them (a collar and a sleeve) are not used. The other two are the connector housing itself, which must be soldered to the outer conductor, and a small pin soldered to the inner conductor. Because the connector is relatively massive, more heat is necessary to solder it to the line than is needed for soldering the loop and the danger of expansion of the teflon dielectric is greater. When the probe has been finished, it is advisable to test its DC resistance with an ordinary ohmeter. The resistance should be zero ideally, but it is common to measure 1 or 2 ohms.

The connector is a plug (i.e., it has internal threads) and when the probe is mated with another fitting, the connector is screwed on like a conventional nut. Unfortunately, the entire probe tends to rotate with this screwing motion and since the small pin is held fast to the mated fitting, the pin tends to be twisted off after a few times. We therefore fitted each probe connector with an adapter (Omni-Spectra Model 21090), thus converting the probe output from plug of the OSSM size to a jack of the OSM size. This adapter was also chosen so that the probe could be connected to a tiny Omni-Spectra mixer; the mixer later proved to be defective, and ultimately still another adapter was used (OSM to type N) so that the probe could be mated with a more common (but larger) coaxial mixer marketed by Scientific-Atlanta, Inc. More complete information on these series of plugs, jacks and adapters can be found in the catalogs of Omni-Spectra, Inc., 24600 Hallwood Court, Farmington, Michigan 48024.

2.2 Synthetic Biological Materials

Because the thrust of our research was the study of probe characteristics when the probe is immersed in a typical biological material, we thought it best to use materials having properties similar to actual specimens. For the purposes of probe calibration it is necessary to duplicate or approximate only the electrical properties of biological materials, since any others, such as specific heat, specific gravity, viscosity, etc., do not influence the probe performances. Moreover, since actual bio-

logical material is perishable, its physical and electrical properties change with time. The probe testing would require several months to complete and we needed materials whose properties would be the same throughout this period. We therefore set out early in the contract to fabricate synthetic substitutes in which the probes could be inserted for calibration.

We obtained recipes with which we could fabricate our own synthetic materials from Professor A. W. Guy of the University of Washington. Guy's thermographic studies had shown that his recipes produced materials with electrical properties that could be adjusted to match those of several classes of tissue. The three that interested us most were for bone, muscle and brain synthetics. Typical properties of the materials, as reported to us by Guy in a private communication, are listed in Table 2-1; the recipes are given in Tables 2-2 and 2-3.

As will be pointed out in a moment, we had a great deal of trouble producing a sample of synthetic muscle and no reliable or repeatable data were obtained using Guy's recipe. (This should not be interpreted as demeaning the recipe; it produces an excellent substitute for its original purpose, but was simply not suitable for our own purposes.) Furthermore, since the recipe for the synthetic brain material had the same ingredients, but in different proportions, we did not even attempt to produce synthetic brain. With each new batch of the synthetic muscle we corrected previous problems only to encounter new ones.

For the transmission line tests the samples had to have the shape indicated in Figure 2-4 and we constructed a mold with a 0.425-inch diameter rod running through it so as to provide the hole for the center conductor of the slab line. The sample was cast in one piece and, after removing it from the mold, we sliced it in half in order to install it in the slab line. The synthetic muscle had the color and consistency of actual flesh, but once inside the slab line it clung to the walls and could not be removed intact.

In the second attempt the sample was again cast in one piece, but after removing it from the mold and cutting it in half, we covered its broad faces with waxed paper.

	Muscle	Brain	Fat and Bone
Specific heat	0.84	0.83	0.29 - 0.37
Specific density	0.97	0.96	1.29 - 1.38
Dielectric constant at 915 MHz	50.63	34.37	5.61
Loss tangent at 915 MHz	0.526	0.442	0.233
Dielectric constant at 2450 MHz	49.61	33.56	4.51
Loss tangent at 2450 MHz	0.333	0.2713	0.187

Table 2-1. Properties of synthetic biological materials reported by Guy

Ingredient	per cent by weight
Water	75.44
Polyethylene Powder	15.20
Super Stuff	8.45
Salt (NaCl)	0.907
Household Detergent	a drop

Table 2-2. Ingredients for Meat (Super Stuff is a product of Whamo Manufacturing Company, California)

Ingredient	per cent by weight
Laminac 4110	85.20
Aluminum Powder	14.50
60 Per cent Methyl Ethyl Ketone Peroxide	0.375
Acetylene Black (100 per cent)	0.24

Table 2-3. Ingredients for Bone (Laminac 4110 is a resin available from Fiberlay, Inc., Seattle)

It then slipped into and out of the slab line easily, but it soon began to shrink and dry out. In subsequent attempts we had to cover all the sample surfaces to keep it from drying out, but in time the waxed paper became saturated. Eventually we found ourselves using plastic food wrapping and casting the sample in two halves. The holes and slots in the sample to receive the probes were obtained by inserting plastic drinking straws in the mold and by leaving the straws permanently embedded in the sample. When we finally came up with a good casting technique, we discovered that after being stored in a refrigerator overnight, the samples tended to flatten out, and thus no longer properly fit into the slab line. In addition, we found that the dielectric constant of the material was high enough that higher order modes, as well a as the desired TEM mode, were being generated within the sample. We therefore abandoned our work with this material and ordered a block of commercial waveguide absorbing material whose properties, according to the manufacturer, were in the range of the desired values.

The commercial absorber was rigid and had much the same appearance and physical characteristics of the synthetic bone samples that we made next, and may very well have been based upon the same kind of recipe. The prime ingredient of the synthetic bone is a resin having a noxious and disagreeable odor and it is virtually impossible to clean any mixing vessels or handling containers that have been used with the resin. We found that it attacked and tended to dissolve our plastic mixing containers and we were forced to use the metal cans instead. Since clean-up is very difficult, it is best to discard the vessel after being used.

The first batch of bone material was cast in a solid block from which we hoped to machine a sample to the dimensions in Figure 2-4. We tried to hasten the curing by placing the batch under an incandescent light bulb overnight, but the additional heat (beyond that generated by the curing process itself) caused the

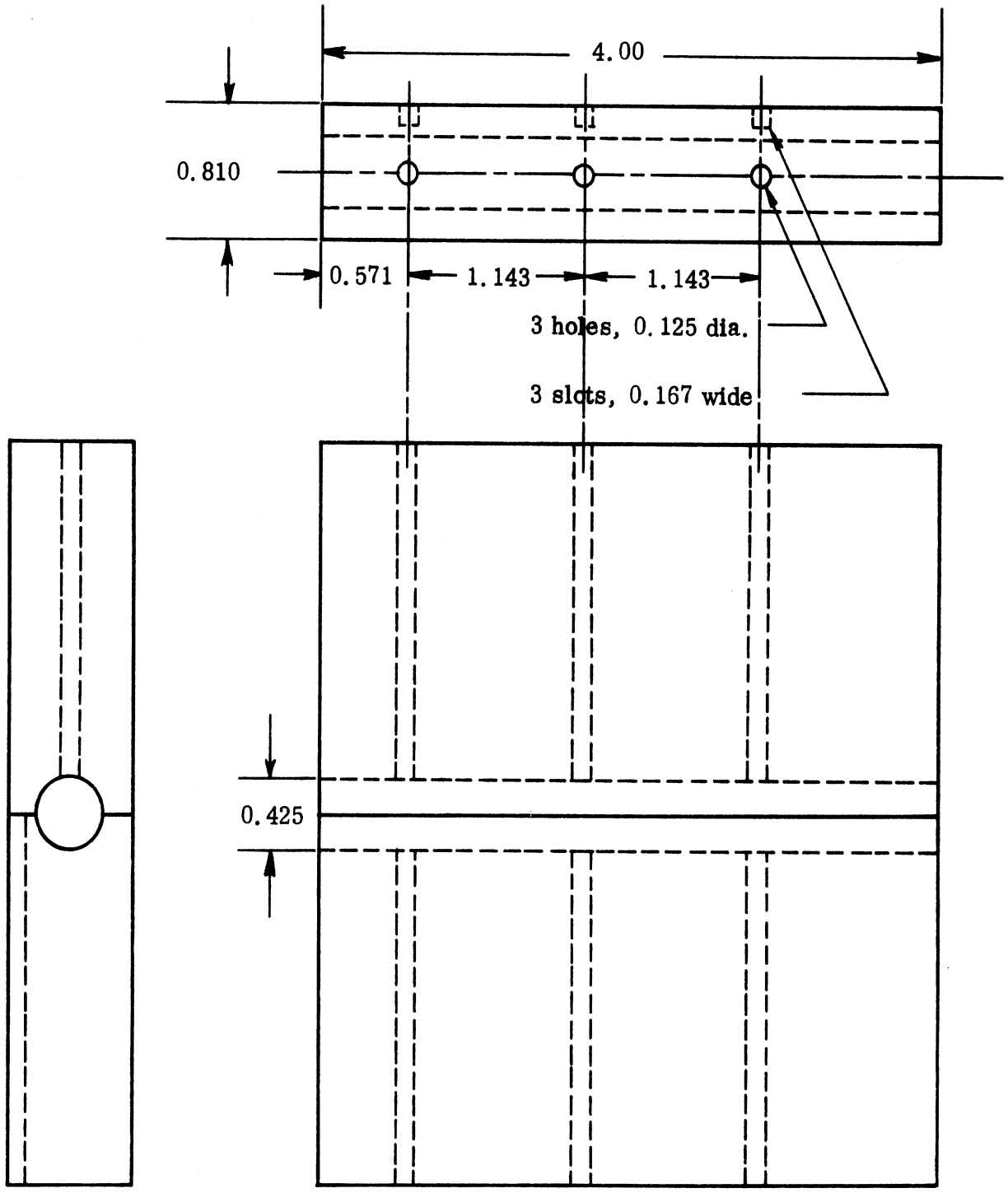

Figure 2-4. Typical size and shape of material samples designed to fit the Hewlett-Packard slab line; dimensions are given in inches.

material to rise at the center like a loaf of bread and it laced the block with deep cracks. The second batch had fewer cracks but they were such that only a short block could be machined from it. Perhaps this was fortunate, because in trying to machine this short sample we found that the large (0.425-inch diameter) hole must be drilled before the rest of the block is surfaced.

The third batch produced a large flawless casting from which we obtained the sample shown in Figure 2-5. Note that holes are drilled in one half while slots are milled in the other; the holes are for the straight probes and the slots for the bent ones, so that the sample halves must be reversed when the probes are switched. The two materials -- the commercial absorber representing brain tissue and the homemade material representing bone -- were machined into virtually identical blocks, all of them precisely 4.00 inches long, and 0.810-inch thick and, when the two halves of each material are assembled, approximately 4.5 inches deep, the depth of the slab line.

Note from Figure 2-5 that the holes are not positioned symmetrically along the length of the sample; this is because we had thought at first that the standing wave pattern within the material would have to be sampled at several positions. The hole spacing was chosen so that, if the sample is reversed end-for-end in the slab line, the reversed hole positions would lie precisely midway between their normal (forward) positions. This would permit us to sample the field structure effectively at six uniformly spaced intervals but at the cost of drilling only three holes (or milling three slots). We did not use this feature, however, because the sliding short circuit method of slipping the standing wave pattern back and forth in the sample was used instead*. Nevertheless, this hole spacing idea was novel.

2.3 Measurements of Dielectric Constants

We were not able to measure the dielectric constants of these long synthetic

*This technique will be discussed in Chapter III.

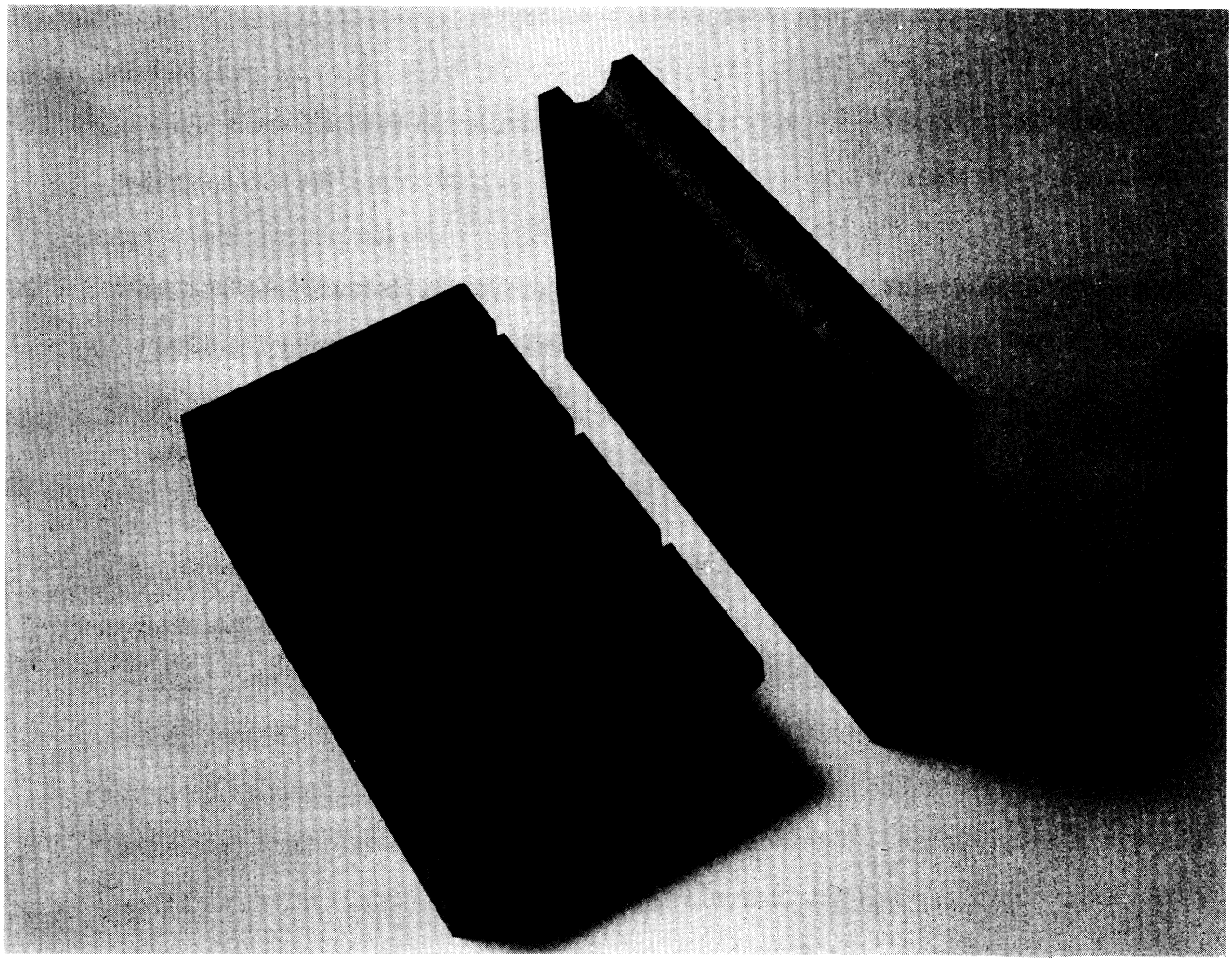

Figure 2-5. Finished sample of synthetic bone.

bone and brain samples because of the difficulties involved in solving the transcendental equations for the reflection coefficients at the front face. The reflection coefficient is easy enough to measure, but if the sample is excessively long, the solution for the real part of the relative permittivity ϵ_r is not unique. Instead we fabricated a pair of thin samples (one each for bone and brain) having the same transverse dimensions as those of Figure 2-4.

In order to measure the dielectric constant of the hard rubber handballs used in the far field testing we had to destroy one to get a sample. The dielectric constant had to be measured in a smaller coaxial line (than the Hewlett-Packard slab line) because the balls were too small to obtain samples large enough for the slab line. Two annular samples were cut from one ball, one being about 1/16 inch thick and the other 1/8 inch thick. These were fitted into a coaxial sample holder and their dielectric constants were about the same as that of the synthetic bone material measured at a lower frequency.

The method by which the dielectric constant of thin slices of material is determined in a TEM line, be it coaxial or a slab line, is shown in Figure 2-6.

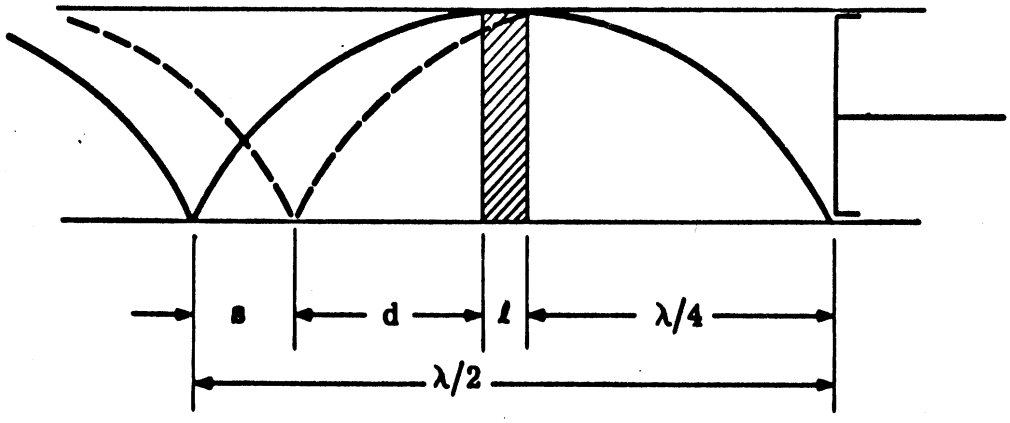

Figure 2-6: A thin sample shifts the null toward the load.

The thin slab (or annulus) is backed by an open circuit, which in turn is actually obtained by positioning a short circuit precisely an odd multiple of a quarter wavelength behind the sample. The input impedance at the front face of the slab is determined by a measurement of the standing wave pattern in front of the sample; specifically the null shift s and the voltage standing wave ratio ρ is measured. The null shift describes how much a null in the pattern shifts toward the load when the sample is inserted into the line and is largely due to the increased electrical length of the sample. Since the impedance is a function of the dielectric constant and the thickness of the slab, the measured impedance is used to deduce the relative permittivity.

The input impedance as obtained from the measurements is

$$Z_{in} = Z_o \frac{\rho \tan kd + i}{\tan kd + i\rho} \quad , \tag{2.1}$$

where Z_o is the characteristic impedance of the empty line (i.e., 50 ohms), and d is the null position in front of the sample and can be found in terms of the shift s

$$d = \lambda/4 - (s + \ell) \quad ,$$

where ℓ is the sample thickness. The open circuit impedance at the front face of the sample is

$$Z_{in} = Z_o \frac{ik\ell}{\gamma\ell \tanh \gamma\ell} \quad , \tag{2.2}$$

where the propagation constant in the material is $\gamma = ik\sqrt{\epsilon_r}$ and ϵ_r is the complex relative permittivity. All we need do is equate (2.1) and (2.2) and solve for γ (or ϵ_r) in terms of the measured values.

The solution is not quite this simple because the unknown appears in the denom-

inator of (2.2) as well as in the argument of a hyperbolic tangent function, thus forming a transcendental equation. It is here that we require the sample to be thin; for if $\gamma\ell$ is small (by virtue of ℓ being small), then the hyperbolic tangent may be approximated by the series

$$\tanh \gamma\ell \cong 1 - \frac{1}{3}(\gamma\ell)^2 + \frac{2}{5}(\gamma\ell)^4 - \frac{17}{315}(\gamma\ell)^6 + \ldots \qquad (2.3)$$

This approximation was used to evaluate (2.2) and only the four terms shown were actually used (that is, powers higher than the sixth were neglected).

Equation (2.2) can be rearranged as

$$\gamma\ell = \frac{Z_o}{Z_{in}} \cdot \frac{ik\ell}{\tanh \gamma\ell} \qquad (2.4)$$

and this form is useful to solve for $\gamma\ell$ by means of an iterative process; Z_o / Z_{in} is first determined from the reciprocal of (2.1) and is thus a known (measured) quantity. The procedure is to then approximate $\tanh \gamma\ell$ by $1 + i\,0$ and to estimate $\gamma\ell$ by the use of (2.4). Then a better approximation of $\tanh \gamma\ell$ is computed from (2.3) which, when used in (2.4) produces a better estimate of $\gamma\ell$. Then (2.3) is used to improve the estimate of $\tanh \gamma\ell$, and so on, until $\gamma\ell$ is as precise as desired. The procedure becomes progressively more lengthy as $\gamma\ell$ grows larger, and is therefore of dubious value for high frequencies and high dielectric constants.

The values of ϵ_r for bone and brain synthetics were obtained for 0.125-inch thick specimens and were obtained with as few as three iterations at 1.0 GHz and as many as 21 at 5.5 GHz. In one instance (for the brain sample at 5.5 GHz), the material was over $\lambda/4$ thick due to the high value of ϵ_r and $\gamma\ell$ could not be accurately computed because the thinness requirement was not satisfied. The results of the

measurements are displayed in Tables 2-4 through 2-6. Note that the properties of our bone sample are similar to those of Guy (cf. Table 2-1), but that our brain sample has smaller dielectric constant. Judging by the trend in $|\epsilon_r|$ for synthetic

Frequency, GHz	ϵ_r	$\lvert\epsilon_r\rvert$	tan δ
1.0	6.16 - i 0.859	6.22	.139
2.5	4.90 - i 0.655	4.96	.134
3.7	4.87 - i 0.548	4.90	.111
5.5	3.61 - i 0.039	3.61	.011

Table 2-4. Measured dielectric constants for synthetic bone (Guy's recipe).

Frequency, GHz	ϵ_r	$\lvert\epsilon_r\rvert$	tan δ
1.0	19.36 - i 21.79	29.15	1.15
2.5	14.25 - i 3.60	14.69	0.253
3.7	15.41 - i 4.94	16.18	0.320

Table 2-5. Measured dielectric constants for synthetic brain (Emerson and Cuming absorber, type HF-680).

Frequency, GHz	ϵ_r	$\lvert\epsilon_r\rvert$	tan δ
5.5	3.06 - i 0.737	3.15	0.241
7.0	3.03 - i 0.211	3.04	0.070
10.0	1.98 - i 0.084	1.99	0.042

Table 2-6. Measured dielectric constants for synthetic bone (hard rubber handball).

bone with increasing frequency as shown in Table 2-4, the values for ϵ_r of the rubber handball at the higher frequencies, as shown in Table 2-6, suggest that the handball material is a more reasonable simulation of fat and bone than brain.

III

PROBE TESTING PROCEDURE

The analysis given in Appendix A shows that the performance of a small loop can be duplicated by the equivalent circuit shown in Figure 3-1 on the following page. As indicated in Appendix A, the loop itself is modeled by a voltage source V_{oc},

$$V_{oc} = -i2\pi fBA, \tag{3.1}$$

that depends only on the magnetic flux density B of frequency f to which the probe is exposed, and the loop area A. The loop impedance Z_p is a function of the conductivity of the metal of which the loop is made, the geometrical configuration of the loop and the medium surrounding the loop.

The open circuit voltage of (3.1) cannot be measured directly because a lossy length of transmission line, represented as the tee network in Figure 3-1, lies between the loop and the detector, and because the detector itself loads down the circuit (i.e., its impedance is not infinite). The input terminals (1) are not accessible, but the output terminals (2) are; thus the source and impedance network to the left of terminals (2) can be represented by the Thevinin equivalent circuit in the lower part of Figure 3-1. The impedance Z'_p can be measured from terminals (2) if the detector is removed, but V'_{oc} cannot be measured without the detector. The voltage appearing across the detector load impedance, however, can be used along with measurements of Z'_p and Z_d to deduce V'_{oc}. We shall not attempt to measure phase, and thus instead of equation (3.1), the measurements are really of

$$V_p = V'_{oc} = CfB, \tag{3.2}$$

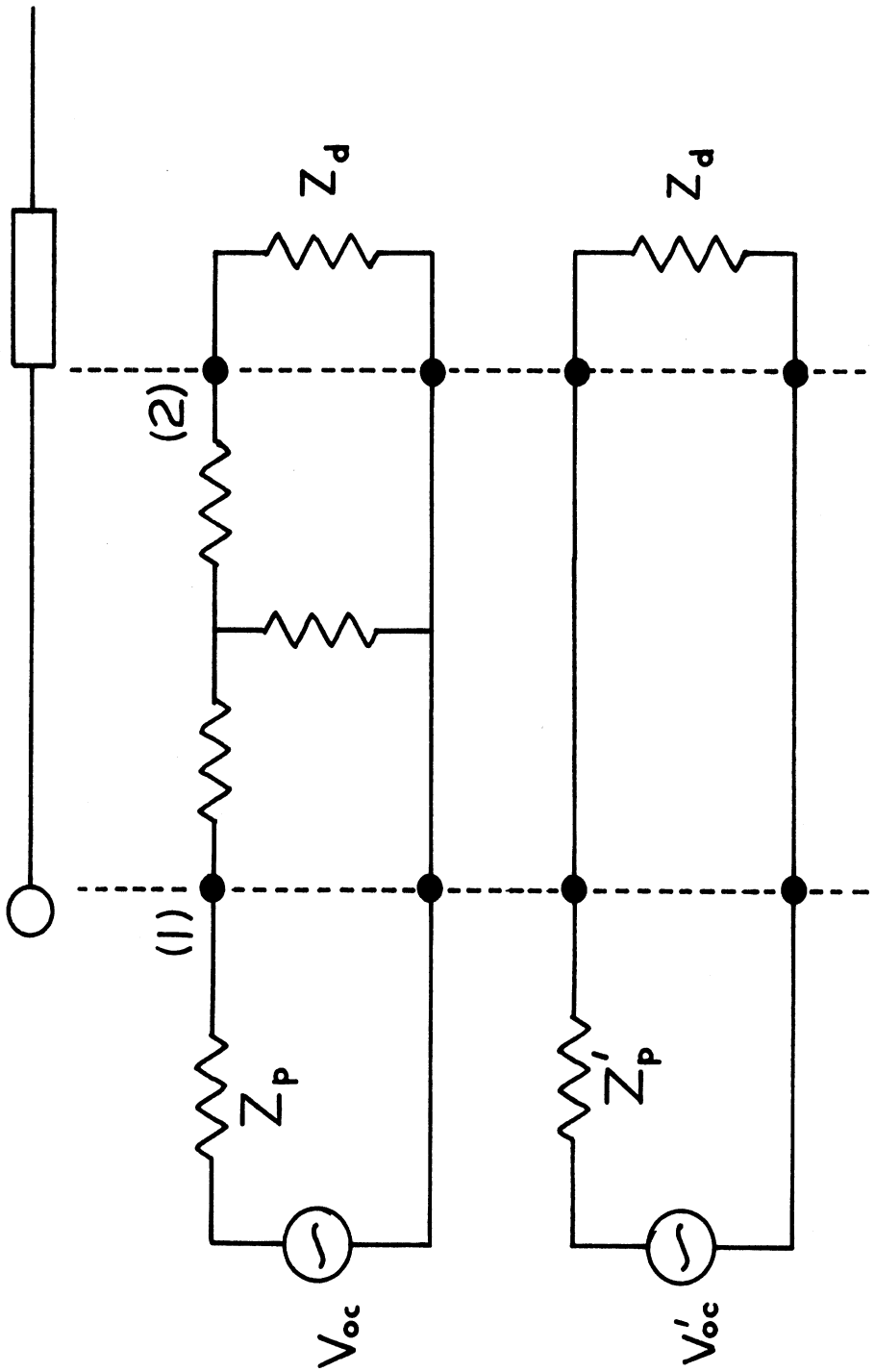

Figure 3-1. Equivalent circuits of probe, probe lead and detector.

where the probe area A and the effects of losses have been absorbed in the coefficient C, but the fundamental dependence on frequency and flux density are explicit.

Equation (3.2) can be solved for C,

$$C = \frac{V_p}{fB} \tag{3.3}$$

and the task we set ourselves was to supply known values of B and f in the synthetic biological specimens and to measure the voltage V_p, thereby evaluating C. We planned to carry out the evaluation in both enclosed and open systems at six frequencies, but due to higher order mode generation within the transmission line samples, this could not be done at the higher frequencies.

3.1 Measurements of V_p

The voltage developed across the detector could not be measured at the frequencies used because it was small and because we used a microwave superhetrodyne receiver to detect the probe signals. The superhetrodyne receiver was not really necessary in the transmission line measurements, but we knew at the outset that the far field work would require it and we resolved to use the same technique throughout.

The receiver indicates only relative power, of course, and this required that the receiver response be calibrated, preferably on the same day (or better, within the hour) that the probe output levels were recorded. The receiver was calibrated by injecting a known signal, obtained by means of directional couplers and precision attenuators, directly into the crystal mixer (the detector), just as a probe would. Several signal levels were used in order to assess the receiver linearity (which turned out to be good) and we terminated each day of probe work with at least one calibration curve for each frequency used. The calibration source was a Boonton

power meter (model 42A) fed by a signal sampled from the transmitted signal by a directional coupler whose coupling had been previously measured.

The receiver calibration curve was used to relate receiver indication to probe output power, but of course it is the detector voltage, not power, that is required. We were obliged to measure both the probe and the detector impedances alone, meaning that the probe and detector had to be disconnected and measured separately. From the two impedance values and the probe output power as indicated by the receiver calibration curve, the probe voltage can be calculated from

$$V_p = Z'_p + Z_d \sqrt{\frac{P}{\text{Real}(Z_d)}} \quad , \tag{3.4}$$

where P is the probe output power. The probe impedances must be measured with the probes embedded in the sample materials, since the dielectric medium affects the impedance. Deducing V_p from a measurement of a power and two impedances is only part of the job, of course; we must also supply known values of magnetic flux density that generate the voltage. This was done in both a TEM transmission line and in free space.

3.2 Transmission Line Measurements

For the transmission line measurements we used a Hewlett-Packard model 805-C slab line. It is a section of transmission line fitted with a sliding probe carriage so that the standing wave pattern due to any load connected to its output port may be measured. It is a transverse electromagnetic (TEM) line, and thus operates like a coaxial line, but the outer conductor is formed by a pair of parallel plates. The spacing of the plates and the diameter of the center conductor have been chosen so that the characteristic impedance is 50 ohms. The slab line is electrically identical to a coaxial line with a very narrow slot but due to the field distribution within the line, the actual slot can be physically quite large.

We chose the slab line as a means of calibration because it is physically large enough that our probes could be comfortably slipped into the line and thus be exposed to the fields inside, yet it was a TEM line. Samples of synthetic biological material were machined to fit into the line so that the probes could be calibrated inside a dielectric as well as in air. Preliminary tests of the slab line showed that it could be relied upon only for frequencies less than about 5.5 GHz; a smaller version of the slab line (model 816A) would have extended the frequency range to above 10 GHz but unfortunately this line was physically too small to accept our probes.

The test equipment arrangement for the enclosed system measurements is shown schematically in Figure 3-2. A small portion of the signal generator output is sampled by means of a directional coupler and is monitored with a power meter; the remainder is fed to the slab line sample holder via a pad (fixed attenuator). The power impinging on the front face of the sample can be calculated from the power meter indication and a knowledge of the coupling coefficient of the directional coupler and the loss through the pad. The output of the slab line is terminated with a sliding short circuit whose purpose will be explained in a moment. The probe is attached to a coaxial crystal mixer which is mounted on an instrument slide so that the probe may be lowered a known depth into any of the holes machined in the sample. The mixer is excited by the local oscillator of a superhetrodyne receiver and the receiver output is monitored by a conventional bolometer audio amplifier (called a standing wave indicator).

Figure 3-3 is a photograph showing the equipment used in a typical measurement. The precision pads used in the testing are in the box at lower left and the thin samples used for measurement of dielectric constant rest on the white styrofoam pads in the center foreground. The instrument slide is just behind the slab line. A close-up of a probe poised just above a sample in the slab line is shown

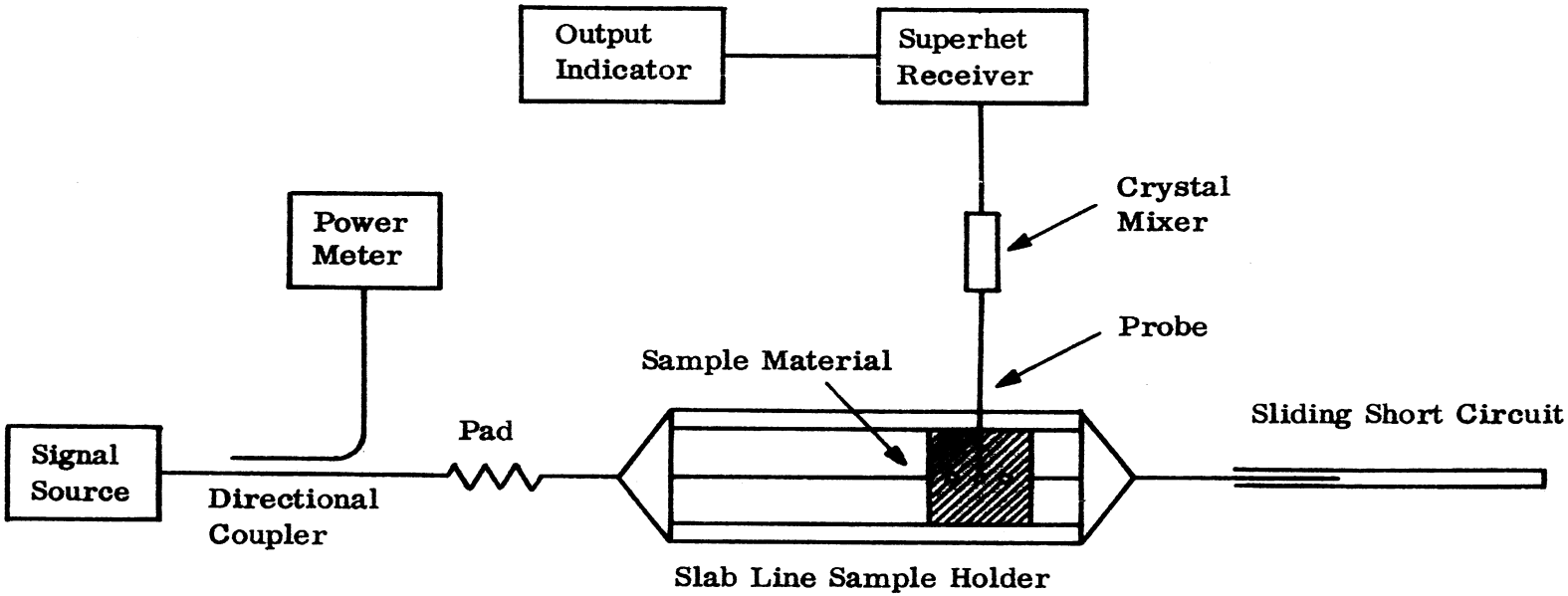

Figure 3-2. Schematic arrangement of test equipment.

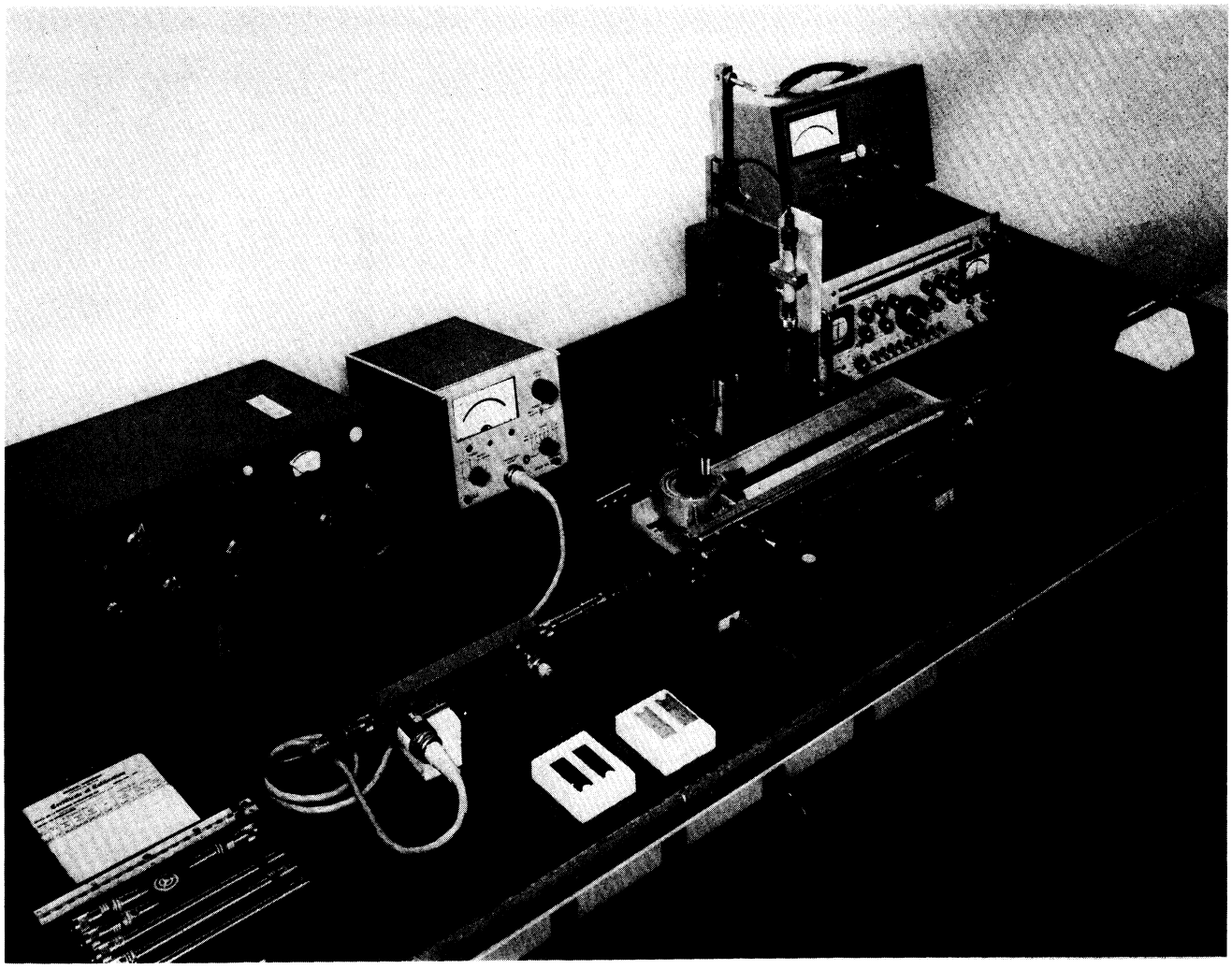

Figure 3-3. Arrangement of test equipment for the measurements.

in Figure 3-4.

Since the air-sample interface reflects some of the incident power in the backward direction, sufficient measurements must be made that the net power entering the sample may be computed. This is simply done by measuring a null shift and the voltage standing wave ratio (VSWR) in the empty portion of the slab line sample holder between the sample and the pad. To obtain the null shift, a short circuit is placed in the slab line against the front face of the sample and the null position is recorded. The short circuit is then removed and the new null position is recorded; the difference in the readings gives the null shift, provided the finite thickness of the short is accounted for. The short circuit we used was a pair of aluminum blocks, precision machined to fit the slab line in the same way the bone and brain samples, the blocks being inserted from above and below the slab line and fitting snugly about the center conductor.

The normalized input impedance associated with the front face of the sample is

$$\frac{Z}{Z_o} = \frac{1 + i\rho \tan ks}{\rho + i \tan ks}$$

where s is the null shift and ρ is the measured VSWR. The voltage reflection coefficient R_E can be expressed as

$$R_E = \frac{Z - Z_o}{Z + Z_o} = \frac{\rho - 1}{\rho + 1} \cdot \frac{i \tan ks + 1}{i \tan ks - 1} \quad . \tag{3.5}$$

If we have measured the power striking the front face of the sample, then R_E will permit us to calculate the power entering the sample across the interface. The electric and magnetic field intensities transmitted across a dielectric interface are

$$\overline{E} = (1 + R_E)\,\overline{E}_i, \quad \overline{H} = (1 - R_E)\,\overline{H}_i,$$

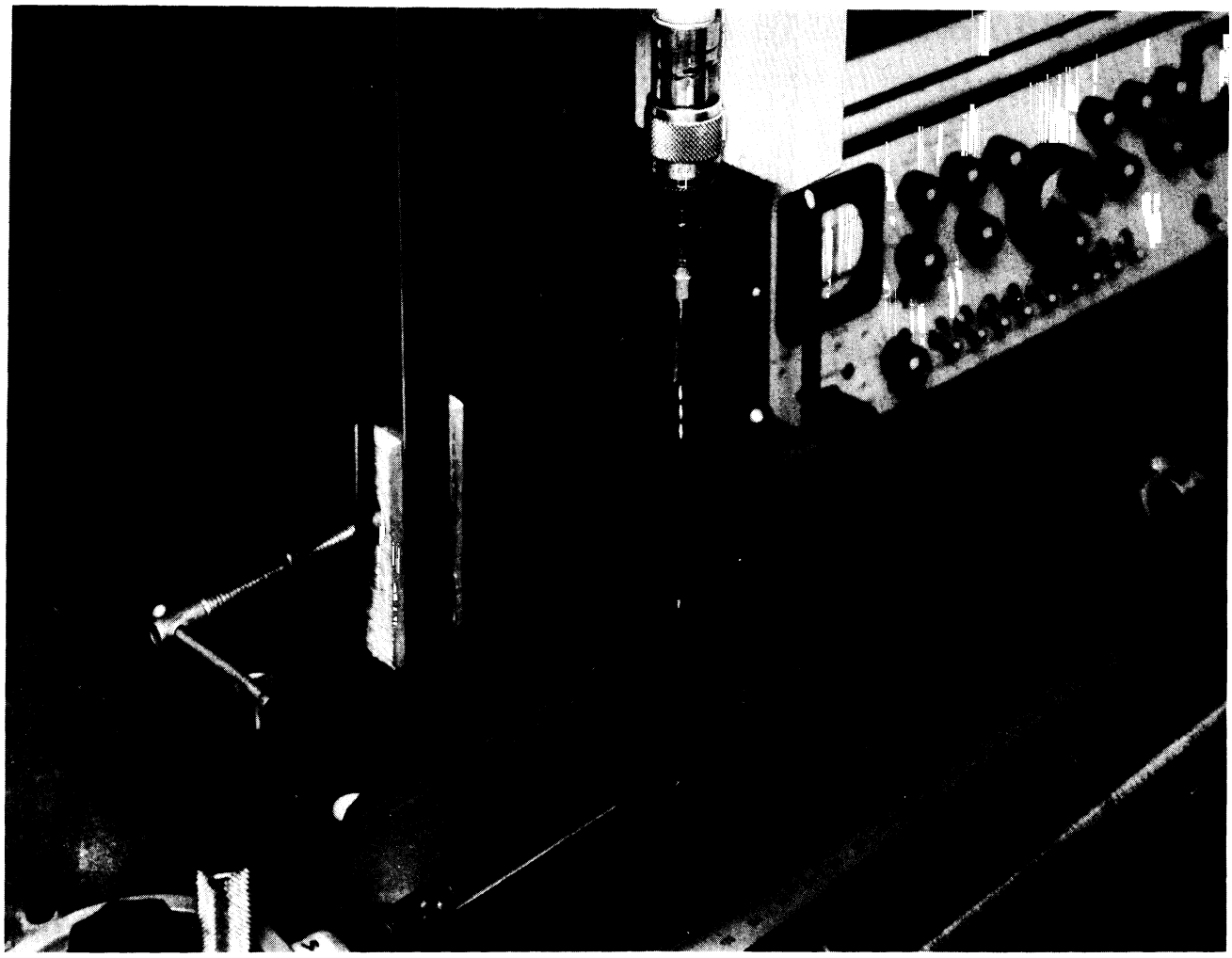

Figure 3-4. Close-up of probe F before being placed in measurement position.

where $\overline{E}_i$ and $\overline{H}_i$ are the incident fields and $\overline{E}$ and $\overline{H}$ are the fields transmitted across the interface.

When these values are used in equation (B17) of Appendix B, the power flowing across a transverse plane located some distance z from the interface is

$$P = \frac{1}{Z} V^2 \left[\text{Real} (1+R_E)(1-R_E^*) \sqrt{\epsilon_r} \right] e^{-i(k-k^*)z} , \qquad (3.6)$$

where Z is the characteristic impedance of the air-filled line, k is the complex propagation constant of the dielectric material, the asterisk indicates the complex conjugate and V is the potential difference between the inner and outer conductors of the slab line. At the interface $z = 0$ and if the incident power P_i is measured just outside the interface, then the power P_t transmitted across the interface is

$$P_t = P_i \left[\text{Real} (1+R_E)(1-R_E^*) \right] . \qquad (3.7)$$

Thus measurements of incident power in the air-filled line in front of the sample and of the complex voltage reflection coefficient of the front face of the sample permit us to calculate the power entering the sample.

Once inside the material, the transmitted power decays exponentially with increasing distance. The decay can be computed from measurements of the dielectric constant of the thin slabs mentioned earlier or it can be deduced from the reduction in the probe output signal as the probe is moved from hole to hole. We chose the latter because six probes were used at each frequency, thus providing more datum points from which to determine the actual power decay; a comparison of the loss along the sample as obtained by both methods is given in Table 3-1. We are thus able to calculate the power flowing past each of the three probe stations in the sample. Our task is now to deduce the magnetic flux densities at the two sites

Frequency, GHz	Bone sample loss, dB/inch via probing	Bone sample loss, dB/inch via ϵ_r	Brain sample loss, dB/inch via probing	Brain sample loss, dB/inch via ϵ_r
1.0	1.02	0.80	2.20	10.21
2.5	1.18	1.71	4.55	5.46
3.7	1.44	2.13	6.62	10.61
5.5	1.57	2.59	9.26	---

Table 3-1. Decay in field intensity as deduced from two methods. The brain sample data are less reliable than that of the bone sample due to possibilities of higher order modes.

in the transverse plane where the bent probes and the straight probes will be placed.

As shown by equations (B16) of Appendix B, we must know the potential difference V between the inner and outer conductors of the line as well as the dielectric constant of the material filling the line (we assume that $\mu = \mu_o$, a valid assumption for biological materials at microwave frequencies). The station-to-station decay in power serves to determine the exponential term in equation (3.6) so that at any station the power P can be calculated with the aid of equation (3.7). Thus (3.6) can be solved for line potential V,

$$V = \sqrt{\frac{ZP}{\text{Real}\left\{(1+R_E)(1-R_E^*)\sqrt{\epsilon_r}\right\}}},$$

which, when inserted in equations (B16), produces

$$B_x = \frac{160.8}{c}\sqrt{\frac{ZP\,\epsilon_r|}{\text{Real}\left\{(1+R_E)(1-R_E^*)\sqrt{\epsilon_r}\right\}}}, \qquad (3.8)$$

$$B_y = \frac{192.9}{c}\sqrt{\frac{ZP\,\epsilon_r|}{\text{Real}\left\{(1+R_E)(1-R_E^*)\sqrt{\epsilon_r}\right\}}},$$

where c is the speed of light in vacuum. Since all quantities on the right sides of equations (3.8) are known or measured, the magnetic flux densities to which the probes are exposed can be computed.

The above analysis is based on the assumption that waves propagate only in the forward direction through the sample, which is tantamount to the assumption that the sample is infinitely long. Because the sample is finite in length, the forward travelling waves will be partly reflected by the rear sample face thus generating backward travelling waves. The net result is that the forward and backward waves will combine to produce a standing wave pattern. Since this pattern is sampled at only three points, instead of continuously, it cannot be known whether a probe samples a maximum, a minimum, or some value between these extremes. This is why the sliding short circuit is provided as a termination behind the sample.

The sliding short serves to shift the standing wave pattern back and forth past the probe. The forward travelling wave amplitude can be obtained by averaging the two values obtained when the short is adjusted for maximum probe output indication and for minimum output indication. Strictly speaking, this is only approximately true because there are two reflections (one from the rear sample face and one from the short circuit), but if the sample is sufficiently lossy, the approximation is good. In the worst case, we estimate that the sliding short circuit technique produces no more than a 9 per cent error in the bone sample measurements at 1.0 GHz; at best, it produces less than 1 per cent error for the brain sample measurements at 5.5 GHz.

3.3 Far Field Measurements

The far field tests were performed in a tapered anechoic chamber, as indicated schematically in Figure 3-5. The output of the signal generator is passed through a precision variable waveguide attenuator before being launched down the axis of the anechoic chamber. The chamber is lined with high quality absorbing material and stray reflected fields in the vicinity of the probe are less than 1 per cent of the incident field strength. The probe and mixer were suspended in the chamber through an opening cut into the ceiling. The far field measurements were carried out at 5.5, 7.0 and 10.0 GHz.

Each probe was tested by recording the signal output for four different orientations obtained by rotating the probe lead about its own axis. For the bent probes the gap was aimed toward, away from and ± 90 degrees from the direction of propagation, and these orientations are also tests of electric field sensitivity. The incident magnetic field was polarized vertically and typically the output indications are all within 0.5 dB of each other (which is considered very good). For the straight probes, horizontal magnetic field polarization was used but, since no magnetic flux threads the loop when the loop is oriented broadside to the incident wave, the signals were very small; ideally they should have been in the noise. When the plane of the loop contains the direction of propagation the signals are typically 20 dB higher than when broadside.

Calibration is performed in two steps, both involving the use of a gain standard horn. First the probe is replaced by the gain standard and, because the horn captures much more energy than the probes, attenuation is increased at the transmitting end to bring the signal level down to the same levels measured for the probes; the attenuator setting is recorded. Then the horn is connected to a power meter and the power is measured. Since the gain of the horn is known and the power is measured, the power density at the probe site can be computed. And since the re-

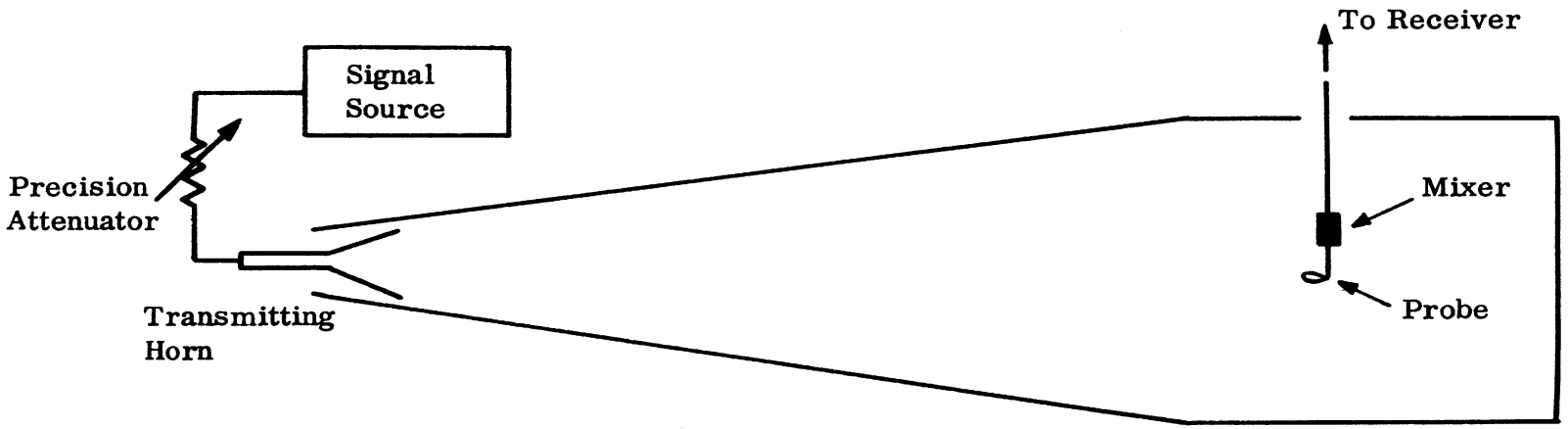

Figure 3-5. A tapered anechoic chamber is used for the free space measurements. The sketch is not to scale.

ceiver response to this power level is also known, the probe output power can be determined. As before, the mixer and probe impedances must be measured to complete the free space probe calibration.

The power extracted from a plane wave by a gain standard horn and delivered to a matched detector is

$$P = \frac{SG\lambda^2}{4\pi} \quad , \tag{3.9}$$

where S is the power density per unit area of the incident plane wave, G is the gain of the horn and λ is the free space wavelength of the radiation. But we know in free space for a plane wave that

$$S = \frac{Z_o B^2}{\mu_o^2} \quad , \tag{3.10}$$

where Z_o and μ_o are the impedance and permeability of free space respectively. Inserting (3.10) in (3.9) and solving for B,

$$B = \frac{\mu_o}{\lambda} \sqrt{\frac{4\pi P}{G Z_o}} \quad . \tag{3.11}$$

Since the gain of the horn can be determined from the theoretical data given by Braun (1956), the magnetic flux density can be computed.

To carry out the testing within a dielectric material in the far field case we used a spherical specimen, since this case can be solved exactly with the least trouble. Rather than undertake the costly machining of synthetic samples into spheres, we purchased a pair of hard rubber handballs at a local sporting goods store. One was deliberately destroyed so that its dielectric constant could be measured, and a hole was drilled in the other so that a probe could be stationed inside.

Figure 3-6 shows the ball mounted on a styrofoam column and how the internal fields were probed. The testing with the dielectric spheres was carried out only with the bent probes D, E and M.

The theoretical basis for determining the fields inside a dielectric sphere under plane wave illumination is summarized in Appendix C. Although a single polarization is transmitted, the magnetic field inside the sphere has radial and angular components:

$$\bar{B}(\bar{r}) = \frac{\mu_o}{Z_o}\sqrt{\epsilon_r} \sum_{n=1}^{\infty} (i)^n \frac{2n+1}{n(n+1)} \Big\{ -\hat{\theta}\, d_n j_n(\rho) P_n^1(0)$$

$$+ i\hat{r} c_n \frac{(\rho j_n(\rho))'}{\rho} P_n^2(0)$$

$$+ i\hat{r} c_n \frac{n(n+1)}{\rho} j_n(\rho) P_n^1(0) \Big\} , \qquad (3.12)$$

where $P_n^1(0)$ is the Legendre function of degree n and order 1 evaluated at zero, $j_n(\rho)$ is the spherical Bessel function of order n, $\rho = kr$, k is the free space propagation constant, $r \leq a$ is the distance from the center of the sphere to the point where the field is to be probed and the primes indicate differentiation with respect to the entire argument.

Only the polarization parallel to the incident polarization is probed, and this is the $\hat{r}$ component sensed by a bent probe. Equation (3.12) is normalized with respect to the incident field intensity B_o in the absence of the sphere for an electric intensity of unity:

$$B_o = \frac{\mu_o}{Z_o} .$$

Thus the internal fields may be calibrated in terms of the incident field in the absence of the sphere, and this in turn is obtained from a measurement in which a gain standard horn is used.

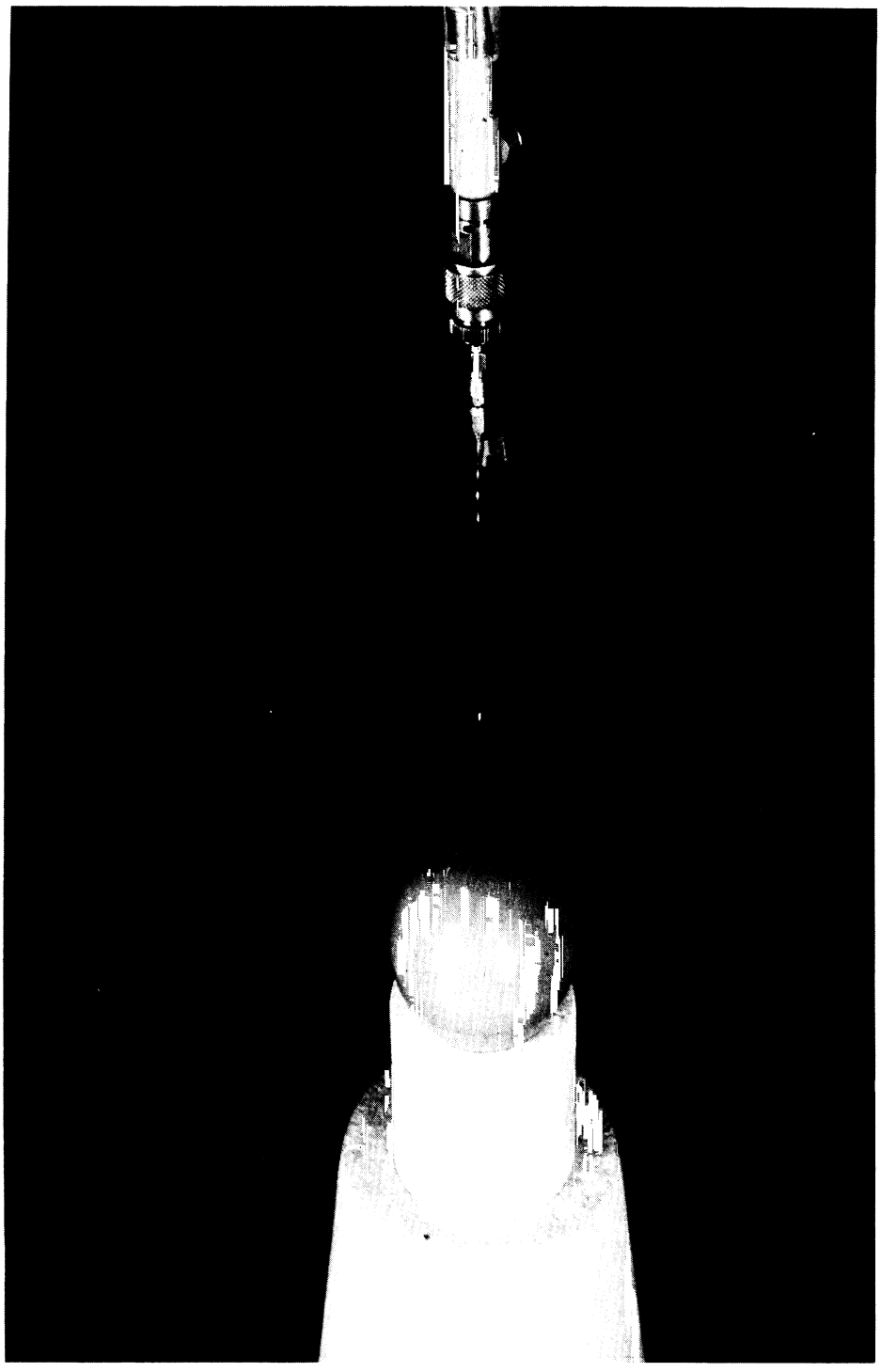

Figure 3-6. Probing the spherical dielectric.

IV

MEASUREMENT RESULTS

4.1 Measured Data

As mentioned earlier, the probe impedances were measured with the probes embedded in the synthetic biological materials, as much as possible in the same way they were embedded when the output power was measured. This required an elaborate set-up in which two slab lines were used, one containing the sample material and the other being the line used to measure probe impedance. The probes were connected one by one to the output port of the air filled slab line with which the standing wave pattern, and thus the probe impedance could be measured. The probe therefore extended away horizontally from the line. Next the sample-loaded slab line was turned on its side and placed on a screw driven fixture such that the center conductor of the line lay in the same horizontal plane as the probe. Then, by careful manipulation of the screw, the sample within the loaded line was slipped over the naked probe.

The probe impedances were measured this way for air, synthetic bone and synthetic brain. The results for air and bone, however, were virtually identical. The impedances are listed in Table 4-1 for the four frequencies used in the slab line system. Note that the measured values are smaller at the lower frequencies and that the probe-to-probe values are fairly consistent. As frequency increases, so do the measured probe impedances, but wide variations are seen at the highest frequency. The imaginary parts of the impedances can be seen to be positive or negative, and this is due to the variations in the electrical lengths of the individual probe leads. As can be seen from Figure 2-1, the probes were not all the same length.

Since a different dielectric material was used in the far field tests, and in a

frequency	probe	air and bone		brain	
		Real	Imag	Real	Imag
	D	0.055	-0.210	0.051	-0.254
	E	0.056	0.107	0.054	0.073
1.0 GHz	M	0.067	0.125	0.063	0.090
	C	0.127	-1.334	0.121	-1.460
	I	0.060	-0.243	0.249	1.751
	F	0.087	-0.944	0.041	0.257
	D	0.106	0.276	0.122	-0.437
	E	0.095	0.691	0.067	-0.071
2.5 GHz	M	0.416	1.894	0.107	0.448
	C	0.848	2.861	0.127	0.716
	I	0.105	0.210	0.062	-0.601
	F	1.103	-3.139	0.648	2.118
	D	0.559	1.586	0.190	0.567
	E	0.537	-1.739	4.332	5.438
3.7 GHz	M	0.235	-0.924	1.996	-3.579
	C	0.429	1.586	0.160	0.541
	I	0.304	0.948	0.035	0.825
	F	0.358	-1.399	11.07	0.532
	D	2.756	-3.227	2.997	-3.014
	E	2.185	-1.061	1.914	-0.899
5.5 GHz	M	0.257	0.429	0.277	0.439
	C	0.150	0.517	0.170	0.500
	I	0.061	-0.761	0.060	-0.743
	F	4.549	0.061	3.817	-0.434

Table 4-1. Measured probe impedances normalized with respect to 50 ohms.

different arrangement, the impedances were somewhat easier to measure in this case. The dielectric sphere was simply slipped over the end of the probe and the probe impedance measured. As in the case of synthetic bone at the lower frequencies, the probe impedance seemed to depend very little on whether the probe was embedded in the rubber ball or not. The measured values are listed in Table 4-2.

As pointed out in Chapter III, it is necessary to measure the detector impedance as well as the probe impedance under the same operating conditions prevailing at the time the probe output power is measured. This means that the crystal mixer detector should be excited by the receiver local oscillator in the same way and at the same frequency used in the probe power measurements. The detector impedance must be measured at the same input port seen by the probe when the two are connected together, consequently this is the port attached to the output terminal of the slotted section used to measure impedance. A signal generator whose output is amplitude modulated is connected to the input terminal of the slotted line.

In order to duplicate the operating conditions, the free terminal of the crystal mixer should be connected to the receiver and the crystal should be excited by the local oscillator at the appropriate frequency. This, however, generates RF within the mixer which then reaches the slotted section; thus there are two waves of two different frequencies in the slotted section travelling in different directions. The result is a very complicated wave structure that cannot be interpreted, consequently, the detector impedance cannot be measured this way. Reasoning that the receiver input is by design a good match, we replaced the receiver with a matched load connected to the free end of the crystal mixer. This resulted in an entirely passive device whose input impedance could be measured and the results are listed in Table 4-3. Note that, even with the mixer terminated in a matched load, the impedances vary as much as ten to one over the frequency band.

frequency	probe	impedance	
		real	imag
5.5 GHz	D	0.701	-1.214
	E	1.676	-1.333
	M	0.257	0.588
	C	0.155	0.560
	I	1.390	2.868
	F	5.050	-0.494
7.0 GHz	D	1.352	1.100
	E	0.169	-0.146
	M	0.105	0.221
	C	0.701	-1.683
	I	0.796	1.265
	F	0.451	0.547
10.0 GHz	D	0.292	0.568
	E	1.035	3.294
	M	0.193	0.457
	C	4.800	-0.024
	I	0.220	-0.450
	F	3.686	-0.857

Table 4-2. Measured probe impedances normalized with respect to 50 ohms.

frequency, GHz	impedance	
	real	imaginary
1.0	0.777	0.177
2.5	1.283	-0.842
3.7	0.255	0.514
5.5	0.147	-0.868
7.0	1.535	-2.472
10.0	0.476	-0.525

Table 4-3. Measured crystal mixer impedance with receiver port terminated with a match load (normalized values).

The data reduction process by which the probe coefficient C is evaluated has been discussed in Chapter III and the intermediate steps will not be given. The transmission line evaluation results are listed in Table 4-4 and the far field results in Table 4-5. In scanning these tables the reader should be aware that, if the probes had indeed been electrically small and had the probe leads been lossless, the value for C should have been in the neighborhood of 23.8 mm^2. Note that the results tend to be lower than this at the lower frequencies and that at the higher frequencies (5.5 GHz and up) the data are more widely scattered. The far field results, perhaps expectedly, are not as consistent as those obtained in the transmission line system. At the higher frequencies, and especially when immersed in the materials of higher dielectric constant, the loops are a significant fraction of a wavelength in size and we cannot expect the "smallness" criterion to be satisfied.

Assessing the coefficient C for a given probe at all six frequencies is awkward using Tables 4-4 and 4-5 and we have therefore rearranged the data in Tables 4-6 and 4-7. Note that Table 4-6 lists only the data for the bent probes while Table

frequency	probe	air	bone	brain
	D	5.4	15.3	6.1
	E	7.2	19.4	7.1
1.0 GHz	M	5.8	25.0	8.3
	C	12.5	33.4	13.8
	I	6.5	14.8	17.9
	F	6.2	26.2	8.6
	D	15.7	16.7	17.9
	E	13.7	14.7	17.5
2.5 GHz	M	30.9	33.6	22.9
	C	55.7	43.7	34.5
	I	13.6	12.6	23.4
	F	71.9	72.6	45.0
	D	36.2	32.2	17.8
	E	24.0	22.0	152.9
3.7 GHz	M	18.8	25.6	155.5
	C	28.7	39.8	22.9
	I	20.5	24.0	21.4
	F	36.7	27.0	285.2
	D	19.9	93.9	112.4
	E	31.1	113.7	103.1
5.5 GHz	M	16.1	14.8	18.0
	C	3.4	-7.5	9.3
	I	9.6	19.5	24.7
	F	17.4	67.0	89.9

Table 4-4. Coefficient C in mm^2 for the slab line measurements.

frequency	probe	in air	in handball
	D	82.2	344.0
	E	235.0	605.0
5.5 GHz	M	51.9	69.0
	C	9.5	--
	I	56.0	--
	F	167.0	--
	D	27.8	22.2
	E	80.7	52.0
7.0 GHz	M	95.1	81.6
	C	23.1	--
	I	4.6	--
	F	40.9	--
	D	2.4	6.4
	E	8.3	23.6
10.0 GHz	M	5.0	14.5
	C	133.0	--
	I	17.5	--
	F	44.5	--

Table 4-5. Coefficient C in mm^2 for the far field measurements. (Probes C, I, F were not used in the handball.)

		slab line			far-field	
probe	frequency	air	bone	brain	air	ball
	1.0	5.4	15.3	6.1	--	--
	2.5	15.7	16.7	17.9	--	--
probe D	3.7	36.2	32.2	17.8	--	---
	5.5	19.9	93.9	112.4	82.2	344.0
	7.0	--	--	--	27.8	22.2
	10.0	--	--	--	2.4	6.4
	1.0	7.2	19.4	7.1	--	--
	2.5	13.7	14.7	17.5	--	--
probe E	3.7	24.0	22.0	152.9	--	--
	5.5	31.1	113.7	103.1	235.0	605.0
	7.0	--	--	--	80.7	52.0
	10.0	--	--	--	8.3	23.6
	1.0	5.8	25.0	8.3	--	--
	2.5	30.9	33.6	22.9	--	--
probe M	3.7	18.8	25.6	155.5	--	--
	5.5	16.1	14.8	18.0	51.2	69.0
	7.0	--	--	--	95.1	81.6
	10.0	--	--	--	5.0	14.5

Table 4-6. Coefficient C in mm^2 for the bent probes.

		slab line			far-field
probe	frequency	air	bone	brain	air
	1.0	12.5	33.4	13.8	--
	2.5	55.7	43.7	34.5	--
probe C	3.7	28.7	39.8	22.9	--
	5.5	3.4	7.5	9.3	9.5
	7.0	--	--	--	23.1
	10.0	--	--	--	17.5
	1.0	6.5	14.8	17.9	--
	2.5	13.6	12.6	23.4	--
probe I	3.7	20.5	24.0	21.4	--
	5.5	9.6	19.5	24.7	56.0
	7.0	--	--	--	4.6
	10.0	--	--	--	17.5
	1.0	6.2	26.2	8.6	--
	2.5	71.9	72.6	45.0	--
probe F	3.7	36.7	27.0	285.2	--
	5.5	17.4	67.0	89.9	167.0
	7.0	--	--	--	40.9
	10.0	--	--	--	44.5

Table 4-7. Coefficient C in mm^2 for the straight probes.

4-7 lists them for the straight probes. A study of these tables shows that among the bent probes, M has the smallest spread in reported values and that among the straight probes, I has the smallest spread.

4.2 Probable Sources of Error

We should point out that although our loops are small, and thus satisfy the theoretical assumption on electrical size (at least at the lower frequencies), they are constructed from a thick enough conductor that we may wonder whether it is the smallest, largest or mean radius that should be used in calculating the loop area A. The mean area would yield $C = 23.8\ mm^2$, as mentioned above, but depending whether the inner or outer loop diameter is chosen, C could take on values anywhere from 14.3 to 40 mm^2. Admittedly some of the values given in Table 4-4 lie outside this range, and they probably include other errors as well, but the question remains which radius is more characteristic.

Probably the largest source of experimental error is in the measurement of impedance, as might be deduced by a comparison of Tables 4-1 and 4-3. In general, there is a strong correlation, the probe coefficient being low when the impedance is low and vice versa. The effect of impedance should disappear from the results, of course, since the test plan has been designed to evaluate what should be a constant for each probe.

Ordinarily, an impedance measurement is a straightforward task but in the probe work, the results depended upon measuring two impedances separately (probe and detector) and then predicting their combined effects. Thus the possible effects of any mutual impedances cannot be accounted for, since the mutual impedance is different or disappears when the two devices are separated. In addition, the impedances were not measured at the same time as was the probe output power, and since the frequency could have changed slightly in the interim, the imaginary parts of the probe and mixer impedances (which are sensitive to small changes in

frequency) could have differed from the apparent values.

The necessity of replacing an active source (the receiver local oscillator) by a matched load could also have a large effect. Although the receiver is designed for broadband service, it is doubtful that the receiver input is matched over the wide frequency range we used. Yet the receiver local oscillator signal produced such interference with the impedance measurements that our only recourse was to replace it with a passive load.

Another possible source of error is the existence of higher order modes, especially at the higher frequencies used in the transmission line measurements. The permissable frequencies at which these modes may exist depend upon the dielectric constant of the material filling the line and their field distributions can be found by solving the boundary value problem. We did not solve the boundary value problem but instead probed the field structures to determine if the magnetic field strength decayed as it should.

Our theoretical analysis showed that the fields should decay at the rate of 33.69 dB per inch as the probe is withdrawn from within the slab line. In most cases this was true, but at 5.5 GHz for bone, and for 3.7 and 5.5 GHz for brain, it was not. This means that not all the measured power was being transmitted through the sample via the TEM mode and consequently that the magnetic flux density, as based on equation (3.4), is not the flux density actually sampled by the probe. Depending upon the precise nature of the higher modes, the total flux can be higher or lower than that given by the TEM analysis, although we suspect that it is lower. Since the computed probe coefficient C varies inversely as the apparent magnetic flux density B, we would expect higher values for C. Inspection of Table 4-4 shows that this indeed happens more often at the higher frequencies, although lower values also occur. The higher order modes do not occur in the far field measurements, however.

The possible errors associated with the sliding short circuit method of deter-

mining the forward travelling wave have already been mentioned; these errors are estimated to be less than 9 per cent for the worst case and is very small for more ideal cases. It is also possible that the samples were not uniform, with the dielectric properties perhaps varying from place to place in the material. This is particularly so with the bone sample since some of the heavier ingredients (i.e., the aluminum powder) tend to settle to the bottom of the sample during the curing period.

Another possible source of error is in the values measured for the coupling factor of the directional coupler and the actual attenuation of pads and other attenuators used in the testing. We feel these errors are gauged in tenths of a dB or less, however, and are not cause for concern. In the far field tests it is a gain standard horn that we use for calibration but again, the theory is sufficiently complete that variations in the gain are not thought to be serious sources of error. Other errors can be attributed to a change in receiver sensitivity in the interval between receiver calibration and probe output power measurements, sheer human error in recording a number different from that indicated by the instruments and in faulty positioning of a probe within the sample.

V

CONCLUSIONS AND RECOMMENDATIONS

Microwave dosimetry is still in the definitive stage and not enough work has been done to reveal whether it is power density or field intensity, or indeed some other electromagnetic quantity, that should be regarded as a dose parameter. In any event, the instrumentation that evolves will depend ultimately upon the use of a small electromagnetic probe acting as an antenna. The specific detection techniques used and calibration procedures to be followed will be influenced by the choice of dose parameter, but the basic probe itself responds to field strength. Implantable probes will have to be calibrated in typical dielectrics at the desired frequencies.

At the present time there is no simple, broadband, implantable probe system available for routine dosimetry work anywhere in the microwave region above 1.0 GHz. Probe systems are, and will continue to be, relatively narrow band, non-implantable, or will require more than routine implementation for some time to come. This is not to say that serious dosimetry cannot be accomplished; it can be and will be, but it will require careful work until some of the problems have been solved.

The problems stem largely from the fact that the three elements of any receiving system -- probe, transmission line, detector -- are poorly matched. Transmission lines and detection systems have been traditionally designed for a nominal 50 ohms, whereas the true impedance of a small probe has a much smaller resistive component and a large reactive component. Maximum sensitivity is synonymous with maximum transfer of power from probe to detector, and this occurs only when the resistive parts of detector and probe impedances are equal, and when their reactive parts sum to zero. While these conditions can be met or nearly met, with

careful designs at selected frequencies, it is a difficult task for any appreciable range of frequencies.

Even if the impedances can be successfully matched, the probe system should be calibrated by subjecting the probe to a known field intensity and to note the output indication of the detection system. This calibration must be repeated if the probe is introduced in a different medium, since the probe impedance is strongly influenced by a new environment; i.e., a probe that has been matched in one medium will not be matched in another. This is also true of frequency; a probe matched at one frequency is not necessarily matched at another. The impact of these variations is that a single calibration curve does not suffice if the probe is to be used for several frequencies in different media.

Probably of greater importance is that the entire system, from probe to detector to output display instrumentation, figures in the calibration procedure. Because of the mismatch problem, a probe calibrated with one system is not likely to remain calibrated in another, even if identical detectors and display instruments are used. This being the case, we obviously could not calibrate our probes for use with another system and instead, we concentrated on individual probe characteristics and how they might be calibrated in a generalized system.

Our research has shown that a major problem is the generation of known values of field strength in dielectrics at high frequencies in enclosed systems. Supplying a known field strength in an enclosed system is probably best done within a simple geometry, such as a rectangular or cylindrical cavity or better, a waveguide, for which the boundary value problem has been or can be solved exactly with a minimum of difficulty. (We chose the slab line and later discovered that even the TEM solution is complicated; we did not attempt to determine the more complex higher order modes.) Having the theoretical solution in hand is not enough, however. The waveguide or cavity should be packed with an isotropic homogeneous dielectric simulating the materials of interest and its electrical properties, especially the losses, should be

well known. Unless the cavity or waveguide dimensions are very small, several modes will be excited and the internal field structure must be probed at sufficiently closely spaced intervals that the relative strength of each significant mode can be established. From a measurement of the total power or voltage supplied to the system, as gauged by a standard power meter or its equivalent, the absolute field strengths may be computed.

The above procedure for an enclosed system suffers the disadvantage that if the dielectric sample is totally enclosed by metal, the walls must be perforated with enough openings that a probe can be stationed at virtually any point inside. An alternative method is to use a far field calibration system employing dielectric spheres illuminated by (essentially) a plane wave. This technique is mechanically much simpler and eliminates the perturbing effect of drilling a multitude of holes in a solid waveguide or solving the higher order mode problems of, say, the slab line. Ideally the sphere should be probed along a radial path and, as can be seen from equation C9, the theoretical field distributions are easily programmable for a high speed digital computer.

Clearly, the calibration of a probe system is not a simple task if the probe is to be embedded in dielectric materials and it would be prudent, unless there are strong indications to the contrary, to minimize the kinds of materials and the number of frequencies at which the actual research takes place. If, for example, one is studying exclusively the biological effects of radiation upon brain tissue, there is no point in calibrating the probe in other materials. Similarly, if only a single frequency is being used (as, for example, in hazardous radiation studies at microwave oven frequencies), then calibration at a variety of other frequencies may not be warranted. But if the whole spectrum of frequencies and materials must be encompassed, calibration will have to be carried out until the basic impedance matching problems have been alleviated.

APPENDIX A: THEORETICAL BASIS OF MAGNETIC LOOP PROBE PERFORMANCE

The response of a small magnetic loop probe to an alternating magnetic flux density B is succinctly embedded in the integral form of Faraday's Law,

$$\oint_C \bar{E} \cdot d\bar{l} = -\frac{\partial}{\partial t} \int_S \bar{B} \cdot d\bar{s} \quad . \tag{A1}$$

Equation (A1) is a statement of the well-known fact that a change in the magnetic flux threading a closed circuit induces a voltage (or current) in the circuit. The surface S need not close upon itself but the contour C is the boundary -- the edge -- of S. The elemental length of contour is $d\bar{l}$ and the elemental area of surface is $d\bar{s}$ and note that these are regarded as vector quantities. Only the induced electric field along the contour and the magnetic flux normal to the surface are included in the calculation. Adopting (and suppressing) a harmonic $e^{i\omega t}$ time dependence converts (A1) to

$$\oint_C \bar{E} \cdot d\bar{l} = -i\omega \int_S \bar{B} \cdot d\bar{s} \quad , \tag{A2}$$

where ω is the radian frequency of the field $\bar{B}$.

Conceptually equation (A2) applies to any loop we may construct, but the integral is difficult to evaluate analytically for any but very small loops. We therefore assume that, even though the loop may be embedded in a medium whose permeability and permittivity are μ and ϵ, the loop is electrically small. For simplicity we orient the loop such that $\bar{B}$ is normal to the plane of the loop and we demand that the surrounding medium be homogeneous and isotropic.

The current induced by the fluctuating field $\bar{B}$ flows on the surface of a circular

conductor of finite size and is therefore a distributed current. We may define a current density J in terms of the total current I distributed uniformly around the perimeter of a circular conductor of radius b,

$$\overline{J} = \frac{I}{2\pi b}\,\hat{\ell} \quad ,$$

where $\hat{\ell}$ is a unit vector along the conductor. The current is the result of a potential gradient $\overline{E}$ and the relation between $\overline{E}$ and $\overline{J}$ is simply $\overline{E} = Z_s \overline{J}$, where Z_s is the surface impedance of the conductor.

Ramo and Whinnery (1960) express Z_s in terms of the magnetic permeability and conductivity of the metal of the conductor, μ_m and σ_m,

$$Z_s = (1+j)\sqrt{\frac{\omega\mu_m}{2\sigma_m}} \quad .$$

King (1956), on the other hand, prefers to define an impedance Z_i normalized with respect to the conductor circumference, and writes

$$Z_i = \frac{Z_s}{2\pi b} \quad ,$$

calling Z_i an internal impedance. In this case the electric field is the product $Z_i I$, whereas in Ramo and Whinnery's notation it would be $Z_s J$. Both, of course, produce the same results. Using King's notation, we have

$$\oint_C \overline{E} \cdot d\overline{\ell} = \oint_C Z_i I \, d\ell = -i\omega \int_S \overline{B} \cdot d\overline{s} \quad . \tag{A3}$$

The only way to extract a signal from the loop is to provide a narrow gap some-

where around the perimeter of the loop and to connect the loop to a transmission line that delivers the signal to a detector. This has the effect of presenting some load impedance Z_L at the gap and across the gap a voltage $V = IZ_L$ appears. The contour integral in (A3) thus has two components, one over the gap width δ and one over the remainder of the contour, $C-\delta$, with the result

$$-i\omega \int_S \overline{B} \cdot d\overline{s} = IZ_L + \int_{C-\delta} Z_i I \, d\ell \quad . \tag{A4}$$

The magnetic flux on the left side of (A4) is the sum of an incident field $\overline{B}_i$ and a scattered field $\overline{B}_S$. The scattered field is generated by the induced current and may be calculated from

$$\overline{B}_S(r, \ell) = \frac{\mu}{4\pi} \nabla \times \oint_C I(\ell) \frac{e^{ikR}}{R} d\overline{\ell} \quad , \tag{A5}$$

where R is the distance between a field point specified by r and a current element specified by ℓ, the current I is a function of ℓ, and $k = \omega\sqrt{\mu\epsilon}$. As required by (A3), the components of $\overline{B} = \overline{B}_i + \overline{B}_S$ normal to the plane of the loop must be integrated over the surface of the loop. With the aid of Stokes' theorem, equation (A5) can be converted to a line integral for this purpose, with the result

$$\int_S \overline{B}_S(r, \ell) \cdot d\overline{s} = \frac{\mu}{4\pi} \oint_C \oint_C I \frac{e^{ikR}}{R} d\overline{\ell} \cdot d\overline{\ell}' \quad , \tag{A6}$$

where the prime distinguishes one loop element from another and R is now the distance between them.

Using (A4) and (A6) in (A3), and remembering that $\overline{B} = \overline{B}_i + \overline{B}_S$,

$$I Z_L + \int_{C-\delta} Z_i I d\ell = -i\omega \int_S \overline{B}_i \cdot d\overline{s} - \frac{i\omega\mu}{4\pi} \oint_C \oint_C I(\ell) \frac{e^{ikR}}{R} d\overline{\ell} \cdot d\overline{\ell}' \quad . \tag{A7}$$

In the general case the current I is a function of position around the loop, but if the loop is very small, I is sensibly constant. This is the so-called low frequency case and permits us to remove the current from within the integral sign. Then (A7) can be written

$$i\omega \int_S \overline{B}_i \cdot d\overline{s} = -I Z_L - I \left\{ \int_{C-\delta} Z_i d\ell + \frac{i\omega\mu}{4\pi} \oint_C \oint_C \frac{e^{ikR}}{R} d\overline{\ell} \cdot d\overline{\ell}' \right\} \quad .$$

Whiteside and King (1964) refer to the reciprocal of the bracketed term as the low frequency loop admittance Y_p; if we let $Z_p = 1/Y_p$ be the low frequency loop impedance, and if $\overline{B}_i$ is essentially constant over, and normal to, the loop,

$$-i\omega B_i A = I(Z_p + Z_L) = I Z_L \left(1 + \frac{Z_p}{Z_L}\right) ,$$

where A is the loop area. Since $I Z_L$ is simply the output voltage V_L at the gap,

$$V_L = -i\omega B_i A \frac{Z_L}{Z_p + Z_L} \quad . \tag{A8}$$

Equation (A8) can be interpreted in terms of the equivalent circuit sketched in Figure A 1. The voltage source is due to the alternating magnetic flux density B_i threading the loop while the loop impedance Z_p is a function of the size and conductivity of the loop and of the properties of the medium surrounding it. The open circuit

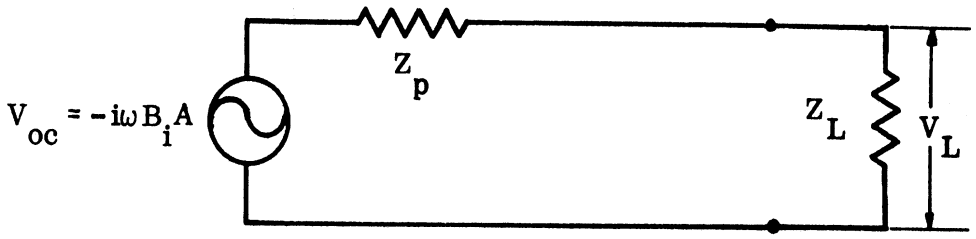

Figure A-1. Equivalent circuit of a magnetic probe loaded with a detector.

induced voltage

$$V_{OC} = -i\,2\pi f B_i A \tag{A9}$$

depends only upon the permeability (μ) of the medium, since $B_i = \mu H_i$. But since μ is sensibly the same as that of free space, we conclude that the induced voltage is independent of the properties of the medium.

Requiring that the loop be electrically small is a restriction only in the sense that (A9) can be written down in simple form. The loop still works where it is electrically large, but a simple expression no longer describes its performance.

APPENDIX B: SLAB LINE FIELD DISTRIBUTIONS

The slab line was introduced over 20 years ago as an improvement over the conventional coaxial slotted line because it has a wide slot that is electrically narrow. Wholey and Eldred (1950) describe the virtues of the line and they emphasize the reduced sensitivity of the probe indication to irregularities in the line as compared to the coaxial line. If the wavelength is greater than some characteristic of the line (which we shall not define), the line supports only a TEM mode. As such, the field distribution within the line is precisely that of the static (d. c.) case.

Wholey and Eldred studied the characteristic impedance of the slab line by using the transformation

$$pz = \arctan w \tag{B1}$$

to map the slab line geometry to a coaxial geometry. The mapping is illustrated in Figure B 1 and note that the circular center conductor of the slab line becomes

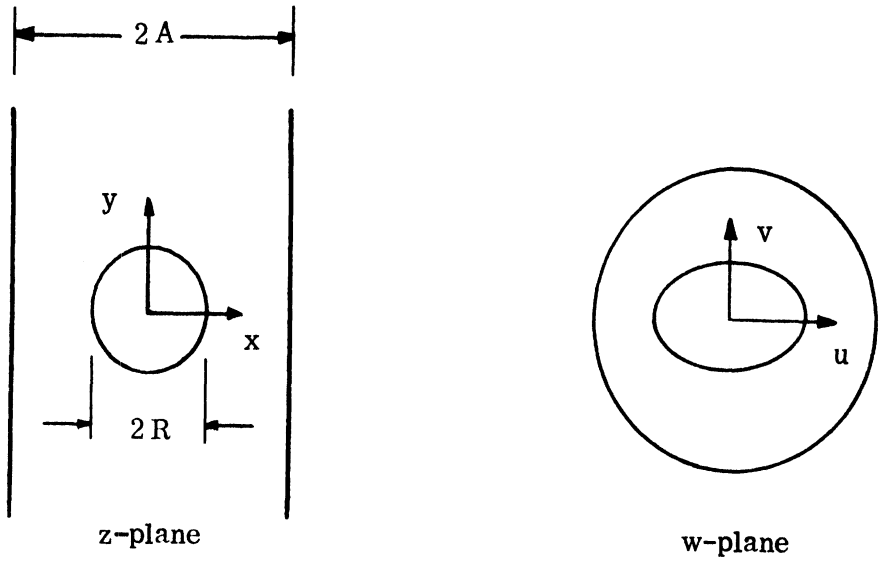

Figure B-1. The slab line is transformed into a coaxial line with an oval center conductor.

an oval conductor in the coaxial line. For the purposes of obtaining the field distributions, we assume the parallel sides of the line extend to infinity, whence the coaxial line produced by the mapping has no slot. The fields in the infinite structure will be slightly different from those in the finite case, but for the dimensions of practical slab lines the differences are negligible.

A coordinate in the z-plane is $pz = px + ipy$ and in the w-plane is $w = u + iv$; the constant p is a scale factor yet to be determined. The transformation (B1) gives u and v coordinates

$$u = \frac{\tan px\,(1-\tanh^2 py)}{1+\tan^2 px\,\tanh^2 py} \quad , \tag{B2}$$

$$v = \frac{\tanh py\,(1+\tan^2 px)}{1+\tan^2 px\,\tanh^2 py} \quad . \tag{B3}$$

The radius r to any point in the w-plane is

$$r^2 = u^2+v^2 = \frac{\tan^2 px+\tanh^2 py}{1+\tan^2 px\,\tanh^2 py} \tag{B4}$$

and $r = 1$ at the outer conductor. The scale factor p can be determined if we require that $u = \pm 1$ and $v = 0$ when $x = \pm A$ and $y = 0$: evidently $\tan pA = \pm 1$, whence

$$p = \frac{\pi}{4A} \quad . \tag{B5}$$

Our task is to determine the static potential function $\phi(r, \theta)$ which satisfies Laplace's equation in cylindrical coordinates. It can be shown that

$$\phi(r,\theta) = V\,\underline{h}\,\ell nr + (mr^2 + nr^{-2})\cos 2\theta\,\underline{} \tag{B6}$$

is such a function, where V is the potential difference between the inner and outer

conductors. In the w-plane, the polar coordinates r and θ are related to u and v by

$$u = r\cos\theta\ , \quad v = r\sin\theta$$

so that (B6) can be expressed as

$$\phi(u,v) = V\left[\frac{h}{2}\ell n(u^2+v^2) + m\,(u^2-v^2) + n\,\frac{u^2-v^2}{(u^2+v^2)^2}\right] . \tag{B7}$$

The boundary conditions on the slab line (in the z-plane) are

$$\begin{aligned} \phi &= 0 \quad \text{for} \quad x = \pm A, \\ \phi &= V \quad \text{for} \quad x = R,\ y = 0, \\ \phi &= V \quad \text{for} \quad x = 0,\ y = R, \end{aligned}$$

which, for the coaxial line, are equivalent to

$$\begin{aligned} d &= 0 \quad \text{for} \quad r = 1, \\ \phi &= V \quad \text{for} \quad u = \tan pR,\ v = 0, \\ \phi &= V \quad \text{for} \quad v = \tanh pR,\ u = 0. \end{aligned} \tag{B8}$$

The first of (B8) immediately implies that $m = -n$, while the last two of (B8) require that

$$\begin{aligned} &\frac{h}{2}\ell n\,(\tanh^2 pR) - m\,(\tanh^2 pR - \coth^2 pR) = 1, \\ &\frac{h}{2}\ell n\,(\tan^2 pR) + m(\tan^2 pR - \cot^2 pR) = 1. \end{aligned} \tag{B9}$$

A simultaneous solution of (B9) for h and m yields

$$h = (t+s)/\Delta\ , \quad m = (\ell n \tanh pR - n \tan pR)/\Delta\ , \tag{B10}$$

where

$$s = \tanh^2 pR - \coth^2 pR,$$

$$t = \tan^2 pR - \cot^2 pR,$$

$$\Delta = t\,\ell n \tanh pR + s\,\ell n \tan pR.$$

The dimensions of the slab line are A = 0.810 inch, R = 0.2225 inch from which the parameters in Table B 1 may be computed.

parameter	value
p, radians/inch	1.939
pR, radians	0.4315
tan pR	0.4604
tanh pR	0.4066
t	-4.505
s	-5.885
Δ	8.619
h	-1.205
m	-0.01443

Table B 1: Pertinent values of some parameters of the slab line.

The electric field intensity is obtained from the gradient

$$E = -\nabla \phi \tag{B11}$$

while the magnetic flux density is obtained from the curl

$$\overline{B} = \sqrt{\mu\epsilon}\,\nabla \times (\hat{z}\phi) = -\sqrt{\mu\epsilon}\;\hat{z} \times \nabla \phi\,, \tag{B12}$$

where $\hat{z}$ is a unit vector in the direction of propagation and μ and ϵ are the permeability and permittivity of the material filling the line.

The characteristic impedance of the line may be calculated from the ratio V/I, where I is the total current flowing on either the inner or outer conductor. If we choose a closed contour C lying somewhere between the inner and outer conductors, then I can be computed from the line integral

$$I = \frac{1}{\mu} \oint_C \bar{B} \cdot d\bar{\ell} \quad ,$$

where $d\bar{\ell}$ is a directed line element along C. If we do this in the w-plane,

$$\nabla \phi(r,\theta) = V \left[\hat{r} \left(\frac{h}{r} + 2m(r+r^{-3}) \cos 2\theta \right) - \hat{\theta} \left(2m(r-r^{-3}) \sin 2\theta \right) \right] ,$$

$$\hat{z} \times \nabla \phi(r,\theta) = V \left[\hat{r} \left(2m(r-r^{-3}) \sin 2\theta \right) + \hat{\theta} \left(\frac{h}{r} + 2m(r+r^{-3}) \cos 2\theta \right) \right] .$$

Along circles of constant radius, $d\bar{\ell} = \hat{\theta} r \, d\theta$, so that

$$I = -V \sqrt{\frac{\epsilon}{\mu}} \int_0^{2\pi} \left[h + 2m(r^2 + r^{-2}) \cos 2\theta \right] d\theta = -2\pi V h \sqrt{\frac{\epsilon}{\mu}} \quad .$$

The impedance of the material-filled line is therefore

$$Z = \frac{V}{I} = -\frac{Z_o}{2\pi h} \sqrt{\frac{\mu_r}{\epsilon_r}} \quad , \tag{B13}$$

where ϵ_r and μ_r are the permittivity and permeability normalized with respect to

those of free space and Z_o is the impedance of free space. The negative sign might appear at first to be incongruous, but h itself is negative so that, for realistic materials, the real part of Z is positive, as indeed it must be.

After a tedious but straightforward calculation, we find the derivatives required by the gradients in (B11) and (B12) to be

$$\frac{\partial \phi}{\partial x} = puV \left(\frac{Q+2v^2}{u^2+v^2} h + 4m \frac{u^2-v^2}{(u^2+v^2)^2} + 2m(Q-2v^2) \left[1 - \frac{1}{(u^2+v^2)^2} \right] \right),$$

$$\frac{\partial \phi}{\partial y} = pvV \left(\frac{Q-2u^2}{u^2+v^2} h + 4m \frac{u^2-v^2}{(u^2+v^2)^2} + 2m(Q+2u^2) \left[1 - \frac{1}{(u^2+v^2)^2} \right] \right), \tag{B14}$$

where

$$Q = \frac{(1-\tan^2 px \tanh^2 py)(1+\tan^2 px)(1-\tanh^2 py)}{(1+\tan^2 px \tanh^2 py)^2} .$$

In the slab line geometry,

$$\bar{E} = -\left(\hat{x} \frac{\partial \phi}{\partial x} + \hat{y} \frac{\partial \phi}{\partial y} \right) e^{i(\omega t - kz)} ,$$

$$\bar{B} = \sqrt{\mu \epsilon} \left(\hat{x} \frac{\partial \phi}{\partial y} - \hat{y} \frac{\partial \phi}{\partial x} \right) e^{i(\omega t - kz)} , \tag{B15}$$

so that $\bar{E}$ and $\bar{B}$ may be computed from equations (B15) by the use of equations

(B14), with the constants h and m given by (B10) and the transformation parameters for u and v given by (B2) and (B3).

Although these expressions are useful for finding field intensities at any point within the slab line, there are two points of special interest. The straight probes sample the magnetic flux density at x = 0, y = R while the bent probes sample the flux density at x = A, y = 0; see Figure B 1. In the first instance u = 0, v = tanh pR, while in the second, v = 0, u = 1.

For the straight probes, $\frac{\partial \phi}{\partial x} = 0$ and

$$\frac{\partial \phi}{\partial y} = pV\left(1 - \tanh^2 pR\right)\left[\frac{h}{\tanh pR} - 2m\left(\tanh pR + \frac{1}{\tanh^3 pR}\right)\right]$$

$$= -4.085\,V \text{ volt/inch}$$

in which the pertinent values in Table (B1) have been used. For the bent probes, $\frac{\partial \phi}{\partial y} = 0$ and

$$\frac{\partial \phi}{\partial x} = 2pV(h+4m) = -4.899\,V \text{ volt/inch}$$

Thus the magnetic flux densitites at the sites in the transverse plane where the straight and bent probes will be placed are

$$B_x = -4.085\sqrt{\mu\epsilon}\,V \quad \text{volt-sec/in/meter},$$

$$B_y = 4.899\sqrt{\mu\epsilon}\,V \quad \text{volt-sec/in/meter},$$

and the electric field intensities are

$$E_y = 4.085\,V \quad \text{volt/inch},$$

$$E_x = 4.899\,V \quad \text{volt/inch},$$

respectively. Converting the constants to the MKS system, and taking the magnitudes (with the understanding that B_x is in the negative x-direction), we have

$$\begin{aligned} B_x &= 160.8\sqrt{\mu\epsilon}\ V \ \text{volt-sec/m}^2, \\ B_y &= 192.9\sqrt{\mu\epsilon}\ V \ \text{volt-sec/m}^2, \\ E_y &= 160.8\ V \ \text{volt/m}, \\ E_x &= 192.9\ V \ \text{volt/m}. \end{aligned} \tag{B16}$$

The power flowing across a transverse plane in the slab line is

$$P = \frac{1}{2}\,\mathrm{Re}\int_S \overline{E} \times \overline{H}^* \cdot \hat{z}\, ds \ ,$$

where $\hat{z}$ is a unit vector along the direction of propagation down the line, $\overline{E}$ and $\overline{H}$ are instantaneous field quantities, the asterisk denotes the conjugate of a complex quantity and the integral is over the transverse region bounded by the conductors in Figure B 1. If the RMS values of $\overline{E}$ and $\overline{B}$ are used, as might be sensed by small probes, then the power flow can be written

$$P = \frac{1}{\mu}\,\mathrm{Re}\int_S \overline{E} \times \overline{B}^* \cdot \hat{z}\, ds \ . \tag{B17}$$

For the purposes of evaluating (B17), it will be convenient to represent the partial derivatives of (B14) as

$$\frac{\partial \phi}{\partial x} = V f(x,y) \ , \quad \frac{\partial \phi}{\partial y} = V g(x,y) \ , \tag{B18}$$

where f and g are real functions, so that, with the aid of (B15), (B17) becomes

$$P(z) = V^2 \left(\mathrm{Re} \sqrt{\frac{\epsilon^*}{\mu}} \right) e^{-i(k-k^*)z} \int_S (f^2+g^2)\, ds, \qquad \text{(B19)}$$

where k is the complex propagation constant of the material in the line. The exponential term is a pure real number that accounts for the decay in power transfer across successive transverse planes; the difference in power levels at any pair of separated planes is the total power deposited in the material between those planes.

As it stands, (B19) is of little value because of the integral. Evaluating the integral is a long and tedious task, as might be guessed from the form of equations (B14), which must be squared and added together, and we merely state the result,

$$\int_S (f^2+g^2)\, ds = -2\pi h.$$

Thus

$$P(z) = -2\pi h V^2 \left(\mathrm{Re} \sqrt{\frac{\epsilon^*}{\mu}} \right) e^{-i(k-k^*)z},$$

and it should be remembered that, since h is a negative number, P(z) is a positive quantity, as indeed it must be. If the permeability of the material filling the slab line is equal to that of free space, then

$$P(z) = \frac{V^2}{Z} \left(\mathrm{Re} \sqrt{\epsilon_r} \right) e^{-i(k-k^*)z}, \qquad \text{(B20)}$$

where Z is the characteristic impedance of the air-filled line.

APPENDIX C: FIELDS INDUCED IN A DIELECTRIC SPHERE

Determining the field structure within a dielectric sphere when illuminated by a plane wave requires that the wave equation be solved in spherical coordinates and that the boundary conditions be satisfied over the air-dielectric interface. The internal fields are represented as the sum of an infinite number of modes, but the contributions of the higher order modes rapidly decrease with the mode order.

Consider a solid sphere of radius a located in the field of an elemental dipole source located some distance b from the center of the sphere. The dipole source is characterized by a current moment c and is oriented along the x-axis; see Figure C-1. The electric field within the sphere due to the external dipole as given by Mason (1972) is the sum of the contributions of an infinite number of modes,

$$\overline{E}(\overline{r}) = -\frac{k\omega\mu c}{4\pi} \sum_{n=1}^{\infty} \frac{2n+1}{n(n+1)} \cdot$$

$$\left[\overline{M}_{o1n}(k_2)\, c_n h_n(\rho_3) + \overline{N}_{e1n}(k_2)\, d_n \frac{(\rho_3 h_n)'}{\rho_3} \right] \tag{C1}$$

where the vector wave functions are (see Chang and Senior, 1967)

$$\overline{M}e_{omn}(k_2) = j_n(\rho) \left[\mp \hat{\theta} \frac{m}{\sin\theta} P_n^m(\cos\theta) \begin{matrix} \sin m\phi \\ \cos m\phi \end{matrix} \right.$$

$$\left. - \hat{\phi} \frac{\partial P_n^m(\cos\theta)}{\partial\theta} \begin{matrix} \cos m\phi \\ \sin m\phi \end{matrix} \right] \tag{C2}$$

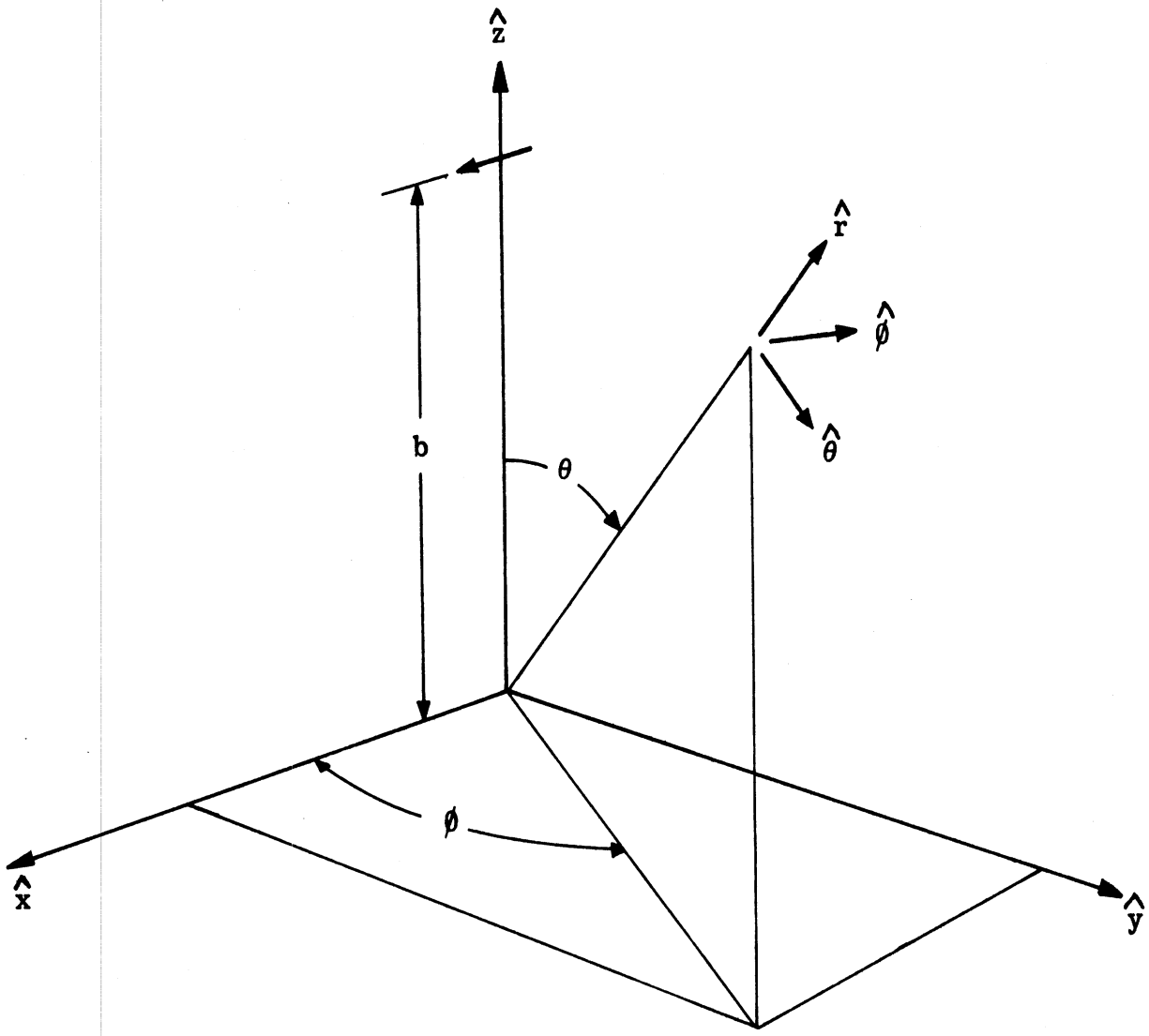

Figure C-1. Spherical coordinate system; the y-directed magnetic flux density is to be probed along the y-axis. An elemental x-directed dipole located at $z = b$ is the source of radiation.

$$\overline{N}e_{o\,mn}(k_2) = \hat{r}\frac{n(n+1)}{\rho} j_n(\rho)\, P_n^m(\cos\theta) \begin{matrix}\cos m\phi \\ \sin m\phi\end{matrix}$$

$$\mp \frac{(\rho j_n(\rho))'}{\rho} \left\{ \hat{\theta} \frac{\partial P_n^m(\cos\theta)}{\partial\theta} \begin{matrix}\cos m\phi \\ \sin m\phi\end{matrix} \right. \tag{C3}$$

$$\left. \pm \hat{\phi} \frac{P_n^m(\cos\theta)}{\sin\theta} \begin{matrix}\sin m\phi \\ \cos m\phi\end{matrix} \right\} ,$$

where $\rho = kr$ (r being the distance from the center of the sphere to a field point and k being the free space propagation coefficient), $\rho_3 = kb$, $k_2 = k\sqrt{\epsilon_r}$ (ϵ_r being the complex relative permittivity of the dielectric material), $j_n(\rho)$ are the spherical Bessel functions of the first kind of order n, $P_n^m(\cos\theta)$ are the associated Legendre functions of degree n and order m, and the primes indicating differentiation with respect to the entire argument.

The mode constants are

$$c_n = \frac{-i}{\rho_1} \frac{1}{(\rho_1 h_n(\rho_1))' j_n(\rho_2) - h_n(\rho_1)(\rho_2 j_n(\rho_2))'} , \tag{C4}$$

$$d_n = \frac{-i\sqrt{\epsilon_r}}{\rho_1} \frac{1}{\epsilon_r(\rho_1 h_n(\rho_1))' j_n(\rho_2) - h_n(\rho_1)(\rho_2 j_n(\rho_2))'} , \tag{C5}$$

where $\rho_1 = ka$, $\rho_2 = ka\sqrt{\epsilon_r}$,

and

$$(\rho Z_n(\rho))' = \frac{\partial}{\partial\rho}(\rho Z_n(\rho))$$

where Z_n is either j_n or h_n, h_n being the spherical Hankel function of the second

kind. We may obtain the results for an incident plane wave by moving the dipole source far away so that b is large. Then ρ_3 is large and we may approximate the Hankel functions by the leading terms of their asymptotic expansions,

$$h_n(\rho_3) \cong (i)^{n+1} \frac{e^{-i\rho_3}}{\rho_3} ,$$

$$\frac{(\rho_3 h_n(\rho_3))'}{\rho_3} \cong (i)^n \frac{e^{-i\rho_3}}{\rho_3} \qquad \text{(C6)}$$

In this case, (C1) can be reduced to

$$\overline{E}(\overline{r}) = \frac{i\omega\mu c}{4\pi b} e^{ikb} \sum_{n=1}^{\infty} (-i)^n \frac{2n+1}{n(n+1)} \cdot \left(-i\, c_n \overline{M}_{o1n}(k_2) + d_n N_{e1n}(k_2) \right) . \qquad \text{(C7)}$$

In equation (C7) the current moment c determines the amplitude and we would like to adjust it so as to normalize the incident plane wave. This amounts to a calibration and if we impose the condition that (C7) be unity when the dielectric constant of the sphere is 1.0 - i 0.0 (which is equivalent to having no sphere at all in the field), then

$$c = -\frac{4\pi b}{\omega\mu} e^{ikb} .$$

Futhermore it is the magnetic flux density $\overline{B}$, not electric field $\overline{E}$, that we desire. From Maxwell's equations we know that

$$\overline{B} = \frac{1}{-i\omega} \nabla \times \overline{E} ,$$

so that the curls of $\overline{M}_{o1n}$ and $\overline{N}_{e1n}$ are needed. It can be shown that

$$\nabla \times \overline{M}_{omn}(k) = k \overline{N}_{omn}(k) ,$$

$$\nabla \times \overline{N}_{emn}(k) = k \overline{M}_{emn}(k) ,$$

whereupon (C7) becomes

$$\overline{B}(\overline{r}) = \frac{\mu_o \sqrt{\epsilon_r}}{Z_o} \sum_{n=1}^{\infty} (i)^n \frac{2n+1}{n(n+1)} \left[d_n \overline{M}_{e1n}(k_2) + i c_n \overline{N}_{o1n}(k_2) \right] , \qquad \text{(C8)}$$

where Z_o is the impedance of free space.

Since we shall probe $\overline{B}$ along the y-axis, $\phi = \pi/2$ and $\theta = \pi/2$. Then (C8) simplifies to

$$\overline{B}(\overline{r}) = \frac{\mu_o \sqrt{\epsilon_r}}{Z} \sum_{n=1}^{\infty} (i)^n \frac{2n+1}{n(n+1)} \cdot$$

$$\left[-\hat{\theta} \left[d_n j_n(\rho) P_n^1(0) + i c_n \frac{(\rho j_n(\rho))'}{\rho} P_n^{(2)}(0) \right] \right.$$

$$\left. + i \hat{r} c_n \frac{n(n+1)}{\rho} j_n(\rho) P_n^1(0) \right] . \qquad \text{(C9)}$$

In arriving at (C9) we have taken $m = 1$ and have used the fact that

$$\frac{\partial P_n^1(0)}{\partial \theta} = - P_n^2(0) .$$

Since we shall probe only the y-component of $\overline{B}$, only the radial component of (C9) is of interest; note, however, that a $\hat{\theta}$ component (which can be thought of as a minus z-component for our geometry) is also present.

For the purposes of computation, it is helpful to know that

$$P_n^1(0) = \begin{cases} (-1)^{\frac{1}{2}(n-1)} \dfrac{1 \cdot 3 \cdot 5 \cdot \cdots \cdot n}{2 \cdot 4 \cdot 6 \cdot \cdots \cdot (n-1)}, & n \text{ odd} \\ 0, & n \text{ even} \end{cases}$$

$$P_n^2(0) = \begin{cases} (-1)^{\frac{1}{2}(n-2)} \dfrac{1 \cdot 3 \cdot 5 \cdot \cdots \cdot (n+1)}{2 \cdot 4 \cdot 6 \cdot \cdots \cdot (n-2)}, & n \text{ even} \\ 0, & n \text{ odd} \end{cases}$$

In practice, of course, n is not permitted to run to infinity, and, depending on the electrical size of the sphere, 20 or 30 terms may be entirely sufficient.

REFERENCES

Bowman, Ronald R., Ezra B. Larsen, Donald B. Belsher and Paul F. Wacker, "Second Progress Report, Electromagnetic Hazards Project," NBS Report 9761, September 1970.

Braun, E. H., "Some Data for the Design of Electromagnetic Horns," IRE Trans. on Antennas and Propagation, Vol. AP-4, No. 1, Jan., 1956; pp. 29-31.

Chang, S. and T.B.A. Senior, "Study of the Scattering Behavior of a Sphere with an Arbitrarily Placed Circumferential Slot," University of Michigan Radiation Laboratory Report No. 5548-6-T, February 1967.

King, Ronold W.P., The Theory of Linear Antennas, Howard University Press, Cambridge, 1956; page 29.

Mason, V. Bradford, "Effect of a Homogeneous Dielectric Sphere on the Radiation from Simple Antennas," Doctoral Thesis, University of Michigan, Department of Electrical and Computer Engineering, 1972.

Ramo, Simon and John R. Whinnery, Fields and Waves in Modern Radio, Second Edition, Wiley and Sons, New York, 1960; page 239.

Whiteside, H. and R.W.P. King, "The Loop Antenna as a Probe," IEEE Trans. on Antennas and Propagation, Vol. AP-12, No. 3, May, 1964; pp. 291-297.

Wholey, W. Bruce and W. Noel Eldred," A New Type of Slotted Line Section," Proc. IEEE, Vol. 38, No. 3, March, 1950; pp. 244-248.

ACKNOWLEDGEMENTS

Much more work was performed than actually described in this final report, but there is neither time nor space to tell the entire story. The author is indebted to Professor Ralph E. Hiatt, Director of the Radiation Laboratory, for attending to omnifarious administrative details and for guidance in assembling the equipment for the experimental work; to Chester Grabowski for his patient and persistent construction of probes, even when we damaged some and asked for more; to Roger Lee and Philip Chan who carried out the measurements and reduced the data under less than ideal conditions; to typist Karen Christiansen who deftly converted an illegible manuscript into legible text; and to Bradford Mason, for providing us with a computer program for calculating the fields inside a dielectric sphere.